NUMERICAL ANALYSIS OF DISSOLUTION BEHAVIOR OF MICRO-ALLOYING ELEMENTS IN LADLE METALLURGY FURNACE

by

Ogochukwu Queeneth Duruiheme

A Thesis

Submitted to the Faculty of Purdue University

In Partial Fulfillment of the Requirements for the degree of

Master of Science in Mechanical Engineering

Department of Mechanical and Civil Engineering

Hammond, Indiana

December 2022

THE PURDUE UNIVERSITY GRADUATE SCHOOL
STATEMENT OF COMMITTEE APPROVAL

Dr. Chenn Q. Zhou, Chair

Department of Mechanical and Civil Engineering

Dr. Nesrin Ozalp, Member

Department of Mechanical and Civil Engineering

Dr. Xiuling Wang, Member

Department of Mechanical and Civil Engineering

Approved by:

Dr. Xiuling Wang

This body of work is dedicated to my family

ACKNOWLEDGMENTS

A special acknowledgment to the National Science Foundation-GOALI (Grant CMMI-2113967) project team for the opportunity to work on this segment, a massive thanks to Steel Manufacturing Simulation and Visualization Consortium (SMSVC) members, Project Technical Committee (PTC) members and Nucor Steel for the sponsorship, continued encouragement, shared industry knowledge and permission to publish this work. Special recognition of CIVS (Center for Innovation through Visualization and Simulation) for the allocation of varying resources to the success of this project. For helping me harness my capability as a student, an engineer, a researcher, and most importantly, a forward-thinker. A note-worthy appreciation to my supervisor Engr. Nicholas Walla and teammate turned friend Xipeng Guo for all input and enlightenment on the subject matter. Thanks to Dr. Tyamo Okosun for constantly addressing concerns and Uzor Chukwunedum for his friendship.

To my advisor, Dr. Chenn Q. Zhou, I'd like to thank you for granting me a seat within CIVS, an exposure that has impacted my pursuit of technical knowledge immensely. Her discipline, proactiveness, and commitment to all she does incite the same in people around her, which is admirable. To my committee members, Dr. Nesrin Ozalp and Dr. Xiuling Wang, I would like to thank you for all your contributions to my academic growth through specific course works under your tutelage and for taking the time to review my thesis.

I extend my love to my husband, mom, and siblings, who have supported my goals and are a source of strength through well wishes and prayers.

All thanks to God for His mercies and guidance throughout the years.

TABLE OF CONTENTS

LIST OF TABLES 7
LIST OF FIGURES 8
ABSTRACT 9
1. INTRODUCTION 10
1.1 Steel modification in ladle metallurgy furnace 10
1.2 Motivations and Objectives 13
2. LITERATURE REVIEW 14
2.1 Gas Stirring 14
2.1.1 Implication of Flow Circulation and Intensity 15
2.2 Alloy Addition 16
2.2.1 Micro-Alloying Elements 17
2.2.2 Shell Formation and Existence Time 18
2.2.3 Dissolution 19
2.2.4 Mixing Time 20
2.2.5 Alloy Recovery 21
2.2.6 Justification 22
3. METHODOLOGY 23
3.1 Flow Model 23
3.1.1 Multiphase Flow 23
3.1.2 Governing Equations 25
3.1.3 Simulation Approach 27
3.1.4 Assumptions 27
3.2 Point Injection Model 27
3.2.1 Simulation approach 27
3.2.2 Model Details 28
3.2.3 Governing equations 28
4. COMPUTATIONAL DETAILS AND BOUNDARY CONDITIONS 31
4.1 Flow Field 31
4.1.1 Geometry and Mesh 31

4.2 Alloy Mixing 35
4.2.1 Mixing 35
5. RESULTS AND DISCUSSION 37
5.1 CFD MODEL VALIDATION WITH PLANT DATA 37
5.2 Flow Field 38
5.2.1 Flow Pattern Analysis 38
5.3 Dissolution and Mixing 38
5.3.1 Particle Behavior 38
5.3.2 Comparison using an Asymmetric Flow Field 42
5.3.3 Single and Dual Plug Mixing Comparison 44
5.3.4 Dissolution Behavior of Different Alloys 45
5.3.5 Mixing 48
5.3.6 Alloy Recovery 49
5.3.7 Bulk Injection 51
6. CONCLUSION 55
REFERENCES 57

LIST OF TABLES

Table 4.1. Physical properties of argon and steel melt. 32
Table 4.2. Properties. 36
Table 5.1. Recovered Copper Concentrations. 37
Table 5.2. Properties of Alloying Elements. 46
Table 5.3. Recovered Copper Concentrations on Parametric Studies. 50
Table 5.4. Recovered Alloy Concentration for all Microalloying Elements. 51
Table 5.5. Recovered Alloy Concentration for Point and Bulk Injection Method. 54
Table 5.6. Computed Cases. 56

LIST OF FIGURES

Figure 1.1.Steel Processing in LMF [1]. 10
Figure 1.2. Injection schematic within the ladle furnace [3]. 12
Figure 2.1. Gas Stirring Process Schematic [6]. 15
Figure 2.2. Alloy Melting Process in Molten Steel [25]. 19
Figure 3.1. Injection Process: (1) alloy entrance (2) shell formation and melting (3) dissolution. 30
Figure 4.2. Ladle mesh. 32
Figure 4.3. Plane Positions. 33
Figure 4.4. Average flow velocities on different planes. 33
Figure 4.5. Concentration of Alloy versus Time [13]. 35
Figure 4.6. Monitoring Points within steel zone. 36
Figure 5.1. Sample location within steel zone. 38
Figure 5.2. Particle behavior at injection points. 39
Figure 5.3. Particle release using point injection. 39
Figure 5.4. Mixing behavior of copper for 1.70 m^3/min total flow rate. 41
Figure 5.5. Vector contour of flow field. 42
Figure 5.6. Mixing behavior of copper for 1.13 m^3/min total flow rate. 43
Figure 5.7. Flow velocities for single and dual plug ladles. 44
Figure 5.8. Mixing behavior of copper for 0.85m^3/min total flow rate. 45
Figure 5.9. Mixing behavior of vanadium alloy for 1.7 m^3/min total flow rate. 47
Figure 5.10. Mixing behavior of vanadium alloy for 1.7 m^3/min total flow rate. 48
Figure 5.11. Concentration profile from same monitoring point stopping at respective mixing times. 49
Figure 5.12. Alloy concentration profile at defined sample points. 51
Figure 5.13. Particle release using bulk injection. 52
Figure 5.14. Mixing behavior of copper alloy for 1.7 m^3/min total flow rate using bulk injection model. 53

ABSTRACT

Due to the difficulty in physically observing the phenomena inside the actual ladle furnace in the industry, to ascertain optimized methodology for high-grade steel production, an investigation was carried out using numerical modeling to simulate the behavior of alloying elements within the liquid steel bulk using ANSYS Fluent 2020 R1 (ANSYS Inc., Pittsburgh, PA, USA). The model solves the governing equations utilized in computing the trajectories of each particle in the discrete phase. Furthermore, a user defined (UDF) code maps the mass of each parcel based on the total amount of alloy injected. The code also defines the total time it takes for the shell formed around the added materials to melt or dissolve. The study consists of a two-step procedure: ladle stirring by argon inert gas injection and mixing study by injecting micro-alloying elements to capture the flow field, turbulence, and species transport occurring during the refining process. A generic dual plug ladle metallurgy furnace, dimensions, and data obtained from Nucor Steel is used to validate the CFD simulation results. Concise parametric studies consist of ladle geometry design adjustments, variations of argon gas flow rates, and different alloying elements. Though the efficiency of the LMF process is quantified using the mixing time, which decreases as initial gas flow rates increase, results from this study show that extremely high charging of ladles is optional in obtaining shorter mixing. Also, particles behave substantially differently when their densities are below or above that of steel, and their melting points and specific heat capacities influence the time it takes for them to melt or dissolve. The overall potential outcome for this study is to improve the mixing practices due to different optimal procedures required by some materials than others.

1. INTRODUCTION

1.1 Steel modification in ladle metallurgy furnace

The ladle metallurgy furnace (LMF) is frequently utilized in refining operations to obtain varying steel grades. It heats steel and improves energy efficiency for the production process, optimizes steel cleanliness, improves quality, and influences cost reduction.

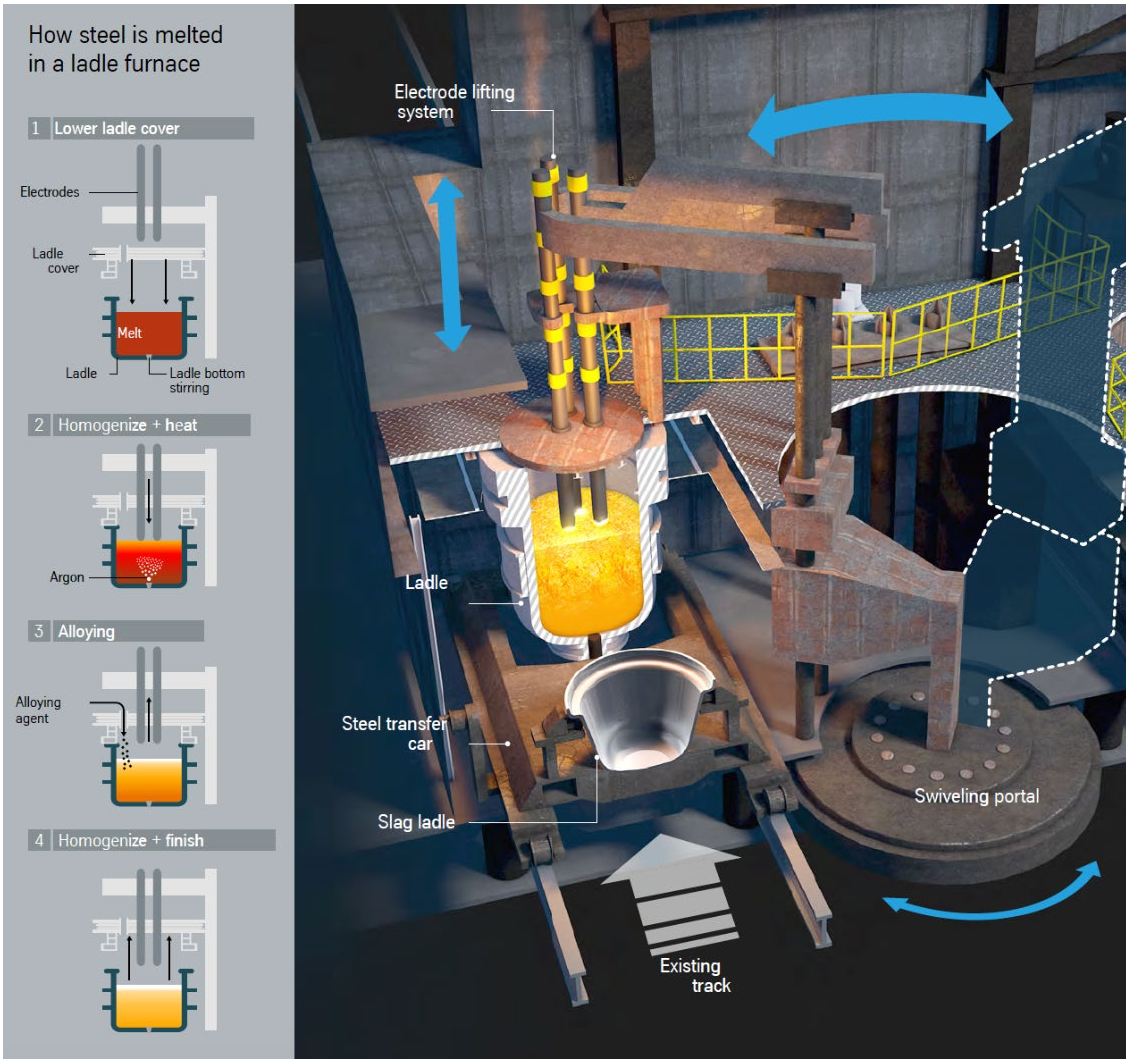

Figure 1.1.Steel Processing in LMF [1].

The LMF makes it possible to differentiate steel melting operations carried out in the electric arc furnace (EAF) from those of treatment and refining. When the liquid steel produced by the EAF is poured into the LMF, an uncontrolled slag layer forms, possessing a different viscosity and lower density than steel with the potential to lessen the rate of the refining process. Fig. 1.1 details the heating of steel inside LMF. The furnace ultimately serves as a reactor for metallurgical operations at the treatment stations, creating high-strength and durable steel grades.

Inhomogeneity elimination, alloy dissolution and inclusion flotation are dependent on the motion of the liquid steel for efficient steelmaking to be achieved. Convection as a result of temperature gradient stimulate this motion; however, it can be slow. Therefore, to create this intense motion externally, gas injection is carried out through tuyere, lances, or plugs [2]. Fig. 1.2 illustrates how injection is carried out from top and bottom of the ladle. During this secondary metallurgy process, the gas flow rates required to stimulate the movement of the metal are regulated according to the needs of the plant operator. However, there are certain restrictions when physically observing the inner workings of the furnace, which has facilitated several model tests by mathematical or numerical methods to study the phenomena of all processes and optimize industry methodology.

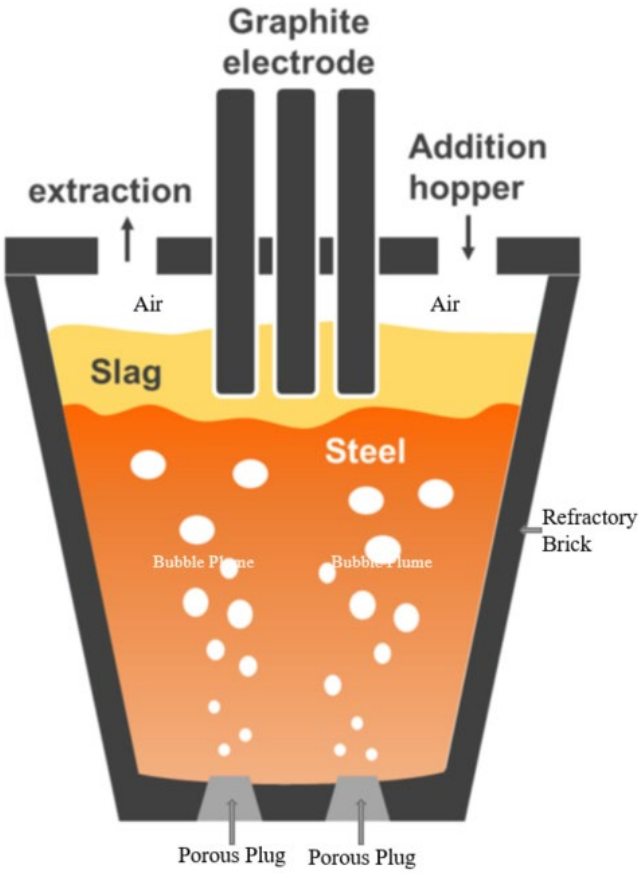

Figure 1.2. Injection schematic within the ladle furnace [3].

1.2 Motivations and Objectives

Metallurgical reactions in the LMF involve adjusting steel chemical compositions and temperatures after tapping to establish uniformity. It relieves the primary steelmaking process, giving way to secondary refining operations aimed at the homogenization of chemical and thermal composition, oxygen removal by killing or deoxidization, superheat adjustment, alloying to balance total chemistry, hydrogen and nitrogen removal by vacuum degassing, decarburization, and inclusion removal or morphology for steel cleanliness.

Uniform diffusivity of alloy properties on the final product after mixing with molten steel prompted this investigation into the dissolution behavior of compounds, such as the micro-alloying elements, due to the resulting high-strength low-alloyed steel (HSLAs). Unlike ferroalloys, the stirring requirements of highly utilized micro alloys like copper, columbium, and vanadium needed for hydrogen-induced cracking suppression, corrosion resistance, and grain refinement have yet to be explored. This could be due to their additions being made in low concentrations or as a mixture with other alloying elements. Parametric studies are conducted on the impact of flow recirculation on the mixing behavior using a single plug ladle at a reduced flow rate and a dual plug ladle with an asymmetric flow rate. Industrial ladle dimensions and material properties validate the model built to obtain simulation results, and computational fluid dynamics (CFD) portrays the particle dissolution mechanism within the ladle metallurgy furnace. In addition, the initial flow field established from gas stirring prior to alloying has also been elucidated in this investigation, as it controls the outcome of the alloying process.

2. LITERATURE REVIEW

2.1 Gas Stirring

Stirring is done to improve refining operations kinetics and achieve growth and possible separation of non-metallic inclusions from molten metal. Of all methods - induction or electromagnetic stirring - gas stirring is one of the most influential and essential, as it contributes to obtaining shortened mixing time and maximum recovery of alloys at an optimal gas flow rate [4]. Plugs play a vital role in attaining effective stirring; however, its disadvantage, common to all steel plants, is their tendency to clog after some time, though this can be monitored and prevented by observing the back pressure in the pipelines. Argon is popularly used to stir molten steel, and its use depends on the type of steel to be refined. It is injected into the molten metal to expedite the rates of various heat and mass transfer-controlled processes such as distribution of heat from the arc, alloy and lime dissolution and mixing, slag–metal reaction, and inclusion flotation, amongst others [5]. Gas bubbles form at the exit of the nozzle, entraining the molten steel into their wake and forming a turbulent plume [6]. However, this depends on the size or amount of gas bubbles input during the injection process, as the stirring intensity creates homogeneity during mixing by increasing the rate of heat transfer and diffusion. Also, bubble flotation acts as a source of momentum source for the molten metal, facilitating a reaction between steel-slag and subsequent homogenization of further additions [7]. The added argon contains very little hydrogen, nitrogen, or oxygen; however, there is no chemical reaction with the liquid steel. The bath temperature and compositions are different at all levels inside the LMF before blowing, so the argon bubbles rising and down force the steel into the same motion, stirring it and promoting uniform composition and temperature of the molten steel [8]. The velocity in the plume zone formed by the gas bubbles, circulating flow rate, and the total time of mixing all correlate as functions of the rate of gas injected, depth of bath, cross-sectional areas of the plume and that of ladle. The circulating flow is significantly influenced by the plume's cross-sectional area, required for mixing [9]. Joo and Guthrie [10] state that it is occasionally necessary to stir the furnace with more than one plug to attain gentle but shorter mixing and avoid explosive effects from vacuum degassing. The stirring phenomena can be seen in Fig. 2.1.

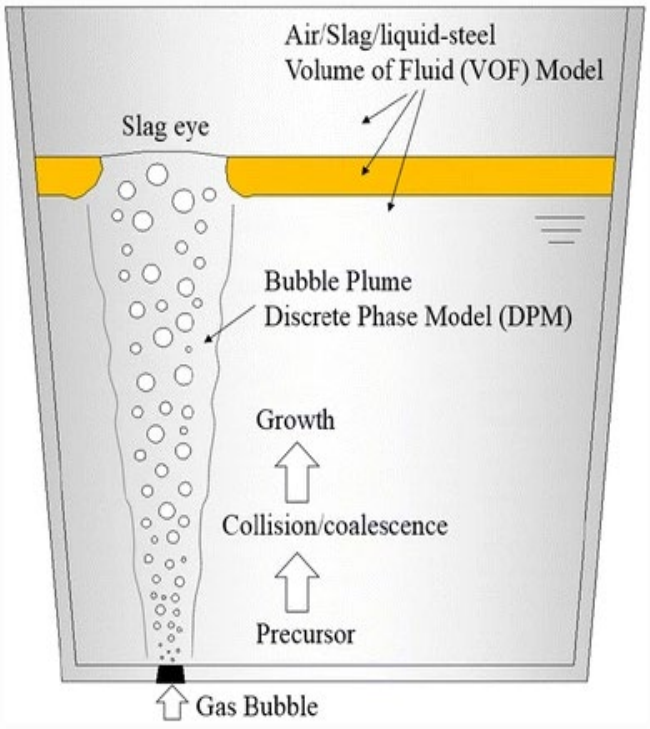

Figure 2.1. Gas Stirring Process Schematic [6].

2.1.1 Implication of Flow Circulation and Intensity

The characteristic feature presiding this phenomenon is the amount of energy that, through the buoyancy of bubbles and their thermal expansion, dispenses when blowing argon into the metal bath [11]. The bubbles generate recirculation and a flow pattern inside the ladle, enhancing the turbulent mixing. Stirring intensity depends on the amount of argon gas entering the ladle furnace, resulting in flow turbulence due to gas bubble expansion as well as the rising of bubbles to the top of the slag. The plume consistently impinges on the slag layer, eventually creating a spout eye [4], exposing the steel to the atmosphere. Widening of the spout eye leads to absorption of the surrounding gas into the molten bath, causing re-oxidation [12]. Entrapment of slag or inclusions in steel occurs in this situation due to stirring intensity. Buoyant energy transfer from the plume influences the motion of the melt, creating a recirculation which is characterized by a central plume zone, central flow along the melt surface, and current projected downwards along the wall of the vessel. The pattern of flow generated are either transient or exhibit inherent instabilities, and the intensity or power of stirring is important in uniform distribution as it significantly affects the

velocity of the steel in the ladle [13]. Stirring intensity can be easily identified by quantifying argon gas injected into the ladle [4].

The time it takes to stir the total volume inside the ladle, equals

$$t_c = \frac{V_L}{\dot{V}_L} \tag{1}$$

where V_L volume of liquid in the ladle; $\dot{V}_L$ circulatory volume flow rate [13].

2.2 Alloy Addition

Attaining desired chemistry in the steelmaking process requires various stages of addition and adjustments to meet specifications. Alloys are trimmed at the LMF to the final specification levels to avoid steel downgrades or diversions to alternate products with lower profit margins. The incremental additions of alloys are conducted cautiously until the required concentrations of various elements are achieved [11]. Some of the chemical or mechanical specifications expected after addition could be steel deoxidation through reaction with oxygen to form oxides absorbed by the slag, increased strength, fatigue, or ductility. In addition, added particles must be submerged in the melt for a substantial time to allow for melting or dissolving. The alloy is fed at a moderate rate into the melt through the slag eye, and the existing gas plume gives good circulation, dispensing the alloy through the melt. Additions to steel are commonly in the form of ferroalloys, which often have melting ranges lower than those of pure elements and are introduced more readily into molten steel [14]. Depending on the density of the particles when compared to that of molten steel, additions may settle or float on the surface, causing oxidation losses or sink to the bottom, reducing the rate of dissolution and recovery; however, the latter varies for different additions [14]. Essential methods for addition in a ladle furnace include bulk additions, dense or dilute phase transport powder injection or wire feeding [15]. For wire feeding, a metal sheath surrounding the alloys protects them from oxidation by the atmosphere and slag while the wire penetrates some distance down into the metal before the sheath cover melts. Bulk addition provides good recovery though particles recovered from wire feeding are highly reproducible. The additions consist of a dual melting stage - comprised of shell dissemination and actual alloy melting- and a mixing stage. Upon addition, a shell freezes over the alloy; however, heat transfer through convection from the

liquid steel remelts the shell. The shell melting is a function of both gas stirring and superheating [2]. The formation of this shell causes the radius of the particle to change during its motion in the melt, influencing the particle velocity by; increasing it if the shell density is greater than alloy density or decreasing it and increasing the drag co-efficient if the heterogeneous zone exists on the surface during shell growth and remelting [16]. These additions are split into classes, with class I being additions with a melting temperature range lower than that of liquid steel and class II being additions with a melting temperature range higher than liquid steel temperature [17].

2.2.1 Micro-Alloying Elements

Micro alloyed steels or high-strength low-alloy steels (HSLA) are materials strengthened by the addition of alloy concentrations in low quantity to mild **low-carbon steel.** Some elements used for this include titanium (Ti), vanadium (V), niobium (Nb), or columbium (Cb), added individually and sometimes in combination with different strengtheners such as copper (Cu), chromium (Cr), boron (B), nickel (Ni), and molybdenum (Mo) to attain desired mechanical properties. These elements are distinguished from other materials due to their inordinately strong effect on the properties and structure of steel while present in low concentrations, generally 0.15% [18]. These elements' strengthening effects make microalloyed steels appropriate for high-strength applications by facilitating grain hardening and refinement [19]. Significant grain refinement obtained as a result of recrystallization retardation by precipitates of carbon-nitride of these microelements strongly influences the final microstructure and properties. HSLA steels are developed based on the inhibition of the recrystallization of the austenite by the precipitates, leading to a reduced grain size after a non-recrystallized austenite transformation [20]. Restraining the added amount of these elements ensures welding performance [21]. Some of the elements analyzed for their dissolution behaviors are copper (Cu), columbium (Cb), and vanadium (V). Cu addition in significant amounts is detrimental; however, when added moderately is beneficial to atmospheric corrosion resistance and produces precipitation-hardening properties. Cb stabilizes elements within stainless steels, possessing a compatibility for carbon with the formation of carbides, evenly dispersed in the steel, further preventing precipitation localizing at grain boundaries. Finally, V retards grain growth at elevated temperatures, increasing strength, hardness, and resistance to shock impact and wear resistance [22].

2.2.2 Shell Formation and Existence Time

A heat sink is created when an alloy is added to liquid steel because there is severe local cooling of the steel in the area due to the temperature contrast, which causes a steel shell to form around the alloy fragment. The alloy particle inside the shell is then pre-heated; if the alloy's liquidus temperature is lower than the solidification temperature of the steel around it, some of the particles may melt before the steel shell is fully remelted [23] as seen in Fig. 2.2. Under the supposition that the impedance to heat transfer within the solidified shell that initially covers the particle surface is zero, the solidification phenomenon around the added alloy can be quantitatively assessed as a function of time. The length of the shell's existence and the amount of heat transferred from the melt to the particle when the shell is still present within the melt are addressed by Zhang and Oeters' [16] mathematical models, which are based on the description of fundamental melting, dissolution, and mixing processes.

The thickness of the shell is determined by the thermal conductivity, specific heat, and particle density [24]. The shell period is influenced by an alloy's low thermal conductivity because it may produce a large thermal gradient within the particle, which lowers the temperature differential between the frozen shell and the alloy's surface. Less heat transfer, a smaller shell, and a shorter shell period are the results of minor temperature differences [13].

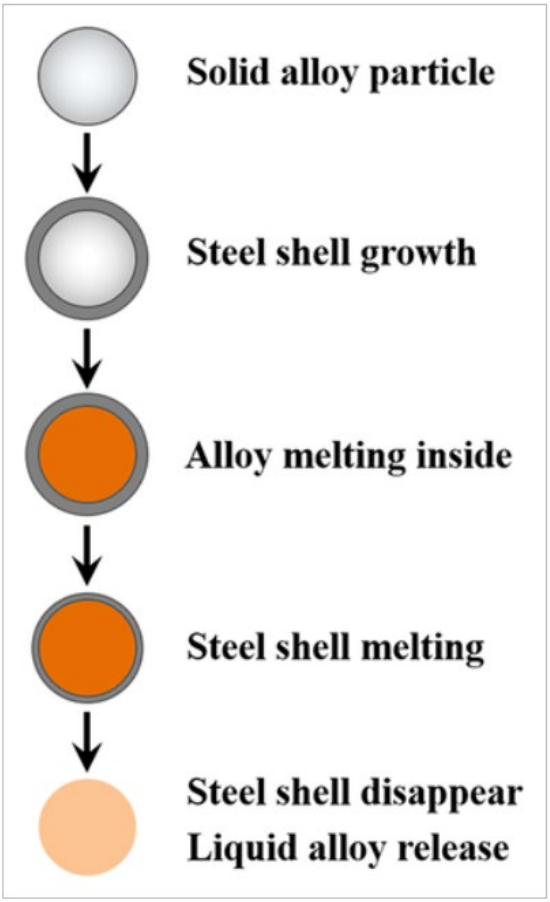

Figure 2.2. Alloy Melting Process in Molten Steel [25].

2.2.3 Dissolution

When considering dissolution or the rate at which it occurs, the size of injected particles, particle melt temperature, steel composition, steel temperature, stirring intensity, and turbulence is essential. Adding large amounts of alloys often results in segregation or inconsistent recovery, though they may aid slag layer penetration. The dissolution rate can be gravely improved by minimizing alloy size. However, it necessitates a larger surface area for the transportation of unwanted gases and moisture and may result in increased dust losses, complicating management [24]. Two processes make up the dissolution process: the surface reaction, which transforms the solid into a liquid, and the boundary layer diffusion, which transports the resultant solute atoms from the interface into the liquid steel [17]. When alloys in different forms, such as lump, granule, or particle, melt or partly dissolve into the melt, they may remain as concentrated volumes of solute surrounded by melt. As they are yet to be thoroughly mixed, concentration c at an arbitrary point

certainly does not equal average concentration c_m. Dissolution in a high-temperature melt should be such that alloy concentrations near the various interfaces should not exceed c_m [15]. Whether alloy particles float, sink, or become entrained in liquid steel depends on the density of the particles [24]. In the melt boundary layer, alloys with melting points greater than temperature of bath dissolve through mass transfer. Alloying elements with high relative density will tend to sink to the bottom leading to a slower dissolution process as the temperature is colder at the bottom and there is lower melt convection [14]. According to Argyropoulos and Guthrie's publication of five theoretical dissolution routes for bulk additions [26], route 1 is where the alloy melts inside the steel, route 2 is where a very thin shell that forms melts so quickly that the alloy does not have time to melt or partially melts in some cases, and route 3 is where a second steel shell forms around the unmelted alloy. However, due to a sizable disparity between the temperature of bath and alloy melting point, the residual solid dissolves quickly. Alloys with high mixing enthalpies are governed by route 4 dissolution, in which they react exothermally with the steel's interior to generate a eutectic liquid that erodes the shell and accelerates bulk melting of the alloy. The phenomenon of mass transfer governs dissolution in route 5. When the shell forms, it is remelted, and the solid then dissolves in the melt by diffusing through a liquid boundary layer and into the bath [13].

2.2.4 Mixing Time

Mixing within chemical and metallurgical process vessels describes the state of agitation, and steel mixing in ladles occurs through convective transport and turbulent eddy diffusion [10]. Used to quantify the mixing efficiency, the mixing time represents the overall period required for materials distributed throughout the ladle to attain a predefined level or percentage of homogeneity. Specific correlations, such as gas injection rate or melt property, are predicted to influence this. Based on liquid phase steady-state energy balance, Sano and Mori's work [9] corroborated total time of mixing as a basic function of bath depth, gas flow rate, and plume zone and vessel cross-sectional areas. Measured mixing time depends on injection and monitoring points [10]. Also, a decrease in the mixing time occurs with increase in the rate of alloy transfer due to high stirring power. However, some experiments, according to Webber [13], have shown certain behaviors where the time of mixing does not decrease with increased stirring power. This could be due to assumptions in route of dissolution because of temperature.

With mixing time expressed as;

$$\tau_{\mathrm{m}} = \frac{C_{\mathrm{l}} R^{2.33}}{Q^{0.33} L} \tag{2}$$

Where L liquid depth (m), τ_{m} bulk mixing time; R mean ladle radius (m); C_{l} empirical constant; Q gas flow rate m^3/s. Mazumdar and Guthrie [37] estimated the constant to be of 29.8 $m^{2/3}/s^{4/3}$ through their investigations of a set of reference conditions.

For an alloy, the change in concentration over time can be computed as;

$$\frac{c(t) - c_{\infty}}{c_0 - c_{\infty}} = \exp(-kt) \tag{3}$$

where the instantaneous concentration $c(t)$ is related to the initial concentration, final concentration c_{∞} , time t and mixing time constant, k

Proportionality factor k' allows for equations 1 and 3 combination, representing mixing time based on circulation and α is the dimensionless concentration term [13].

$$t_{\mathrm{mix}} = k' t_{\mathrm{c}} \ln\left(\frac{1}{\alpha}\right) \tag{4}$$

2.2.5 Alloy Recovery

The slag and metal-slag mixture cause significant metal losses in some facilities. Producers may depend on the profitability of low-cost metal-from-slag products whether demand is high, or prices are low [27]. Economically speaking, alloying compounds are necessary to produce high-quality goods with remarkably repeatable mechanical qualities. Though dependent on factors such as type of additive, alloying methods, or melting techniques, recovery of these alloys is affected by alloy oxidation. It has been proposed that the alloy recovery depends on the alloy's density, dissolution rate, and level oxygen dissolved in melt. Due to the possibility that refractory oxide may form on the alloy surface, oxygen augmentation decreased the amount of alloy that could be recovered and inevitably slowed the dissolution rate of alloys with melting points higher than steel [24]. Argyropoulos [17] defines recovery mathematically as:

$$R = f(u, \rho, [O]) \quad (5)$$

where R is recovery, u is solution rate, ρ is density and [O] is dissolved oxygen on liquid steel.

2.2.6 Justification

As the stirring requirements of these micro alloys are not known, the model created for this study is material specific as it solely identifies each alloy's critical time of dissolution based on defined properties and controls the release of particle mass and their injection time into the bath, in order to correctly simulate the dissolution process. Also, the overall period required for the distributed materials to attain a predefined level or percentage of homogeneity is considered. Recoveries of these alloys after a specific time are compared against plant data using exact sample points.

3. METHODOLOGY

Numerically exploring flow and alloy addition modeling involves defining factors influencing the physical process and flow regime. It is expected that the phases share space proportionally to their volume fractions and that the concept of phase volume fraction is taken into consideration. These can be satisfied by continuous space- and time-functions in which the sum of the volume fractions equals 1. In the momentum equations, forces between gas phase and liquid phase interact and are regarded as source terms for momentum exchange. These equations must be changed to take the phase volume fraction into account [28].

3.1 Flow Model

3.1.1 Multiphase Flow

Mathematical models surrounding multiphase flow investigation relay a few complexities. The flow model developed to simulate gas-stirring in a ladle describes the hydrodynamics of activities, such as bubble size distribution and interfacial forces between them, their density and diameter. The phases involved in the simulation are air, slag, and steel with the injected argon gas. The volume of fluid (VOF) model is implemented in this multiphase solution to elaborate and track interface behavior in all three phases. The discrete phase model describes the tracking of the bubble movement, including buoyancy, drag, virtual mass, and pressure gradient forces [6]. Few assumptions were made for simplification. VOF model and DPM are coupled, resulting in air-argon-slag-steel interface consideration as the gas bubble expansion influences the multiphase flow field [29].

VOF Model

By monitoring the free surfaces between the liquid steel, slag layer, and air, the volume of fluid consideration models two or more immiscible fluids. By figuring out a continuity equation for the volume fraction, it is possible to follow the transitions between phases. The continuity equation has the following form for the qth phase:

$$\frac{1}{\rho_{\mathrm{q}}}\left[\frac{\partial}{\partial t}(\alpha_{\mathrm{q}}\rho_{\mathrm{q}}) + \nabla\cdot(\alpha_{\mathrm{q}}\rho_{\mathrm{q}}\vec{u}_{\mathrm{q}})\right] = 0 \tag{6}$$

Where the volume fraction is α_{q} constrained by $\sum_{q=1}^{n}\alpha_{\mathrm{q}} = 1$. q represents the phases (air, slag and steel). The model's phases do not overlap, and the volume fractions in each control volume added together equal one.

$$\alpha_{steel} + \alpha_{slag} + \alpha_{air} = 1 \tag{7}$$

The various phases share volume averaged values, and mixing attributes are given by:

$$\rho = \alpha_{steel}\rho_{steel} + \alpha_{slag}\rho_{slag} + \alpha_{air}\rho_{air} \tag{8}$$

$$\mu = \alpha_{steel}\mu_{steel} + \alpha_{slag}\mu_{slag} + \alpha_{air}\mu_{air} \tag{9}$$

The velocity field is assumed to be shared by all phases when the VOF model is applied, and the entire domain is solved for a single momentum equation.

DPM

The gas bubble is treated as a discrete phase and the trajectory is predicted by integrating the force balance on it, which is written in a Lagrangian reference frame. This force balance equates the bubble inertia with the forces acting on the bubble, and it can be described as:

$$\frac{\mathrm{d}\bar{u}_{\mathrm{p}}}{\mathrm{d}t} = F_{\mathrm{D}}(\vec{u} - \vec{u}_{\mathrm{p}}) + \frac{\vec{g}(\rho_{\mathrm{p}} - \rho)}{\rho_{\mathrm{p}}} + \vec{F} \tag{10}$$

Where $\vec{F}$ is the additional acceleration term representing both pressure gradient and virtual mass forces, described as:

$$\vec{F}_{\mathrm{VM}} = C_{\mathrm{VM}}\frac{\rho}{\rho_{\mathrm{p}}}\left(\vec{u}_{\mathrm{p}}\nabla\vec{u} - \frac{\mathrm{d}\bar{u}_{\mathrm{p}}}{\mathrm{d}t}\right) \tag{11}$$

$$\vec{F}_{\mathrm{PG}} = \frac{\rho}{\rho_{\mathrm{p}}}\vec{u}_{\mathrm{p}}\nabla\vec{u} \tag{12}$$

$F_{\mathrm{D}}(\vec{u} - \vec{u}_{\mathrm{p}})$ represents drag force per unit bubble mass, $\vec{u}$ is fluid velocity, $\vec{u}_{\mathrm{p}}$ is bubble velocity and C_{VM} represents virtual mass factor of 0.5 [6].

3.1.2 Governing Equations

Mass Conservation:

$$\frac{\partial\rho}{\partial t} + \nabla\cdot(\rho\vec{u}) = 0 \tag{13}$$

where ρ is the density of the mixture, t is time, and $\vec{u}$ is the local velocity.

Momentum:

$$\frac{\partial}{\partial t}(\rho\vec{u}) + \nabla\cdot(\rho\vec{u}\vec{u}) = -\nabla p + \nabla\cdot[\,\mu(\nabla\vec{u} + (\nabla\vec{u})^{T})] + \rho\vec{g} + F_b \tag{13}$$

where p is the local pressure, μ is the viscosity, $\vec{g}$ is the acceleration due to gravity, F_b is the force from bubbles.

Turbulence eddy viscosity:

$$\mu_{\mathrm{t}} = \rho C_{\mu}\frac{k^2}{\epsilon} \tag{15}$$

In terms of the mean strain and rotation rates, angular velocity, and turbulence fields (k and ϵ), inertial sublayer within the equilibrium boundary layer has a constant C_{μ} of 0.09 [30].

Turbulent random walk model for fluctuating component of the particle velocity:

$$\underline{u'}_{\mathrm{b,i}} = \varsigma\sqrt{2k/_{3\underline{e}_{\mathrm{R}}}} \tag{16}$$

Random eddy lifetime:

$$\tau_{\mathrm{e}} = -C_{\mathrm{L}} \frac{k}{\varepsilon} \log_{10} r \tag{17}$$

Bubble trajectories:

$$\underline{x}_{\mathrm{b,i}} = \int \left(\underline{u}_{\mathrm{b,i}} + \underline{u'}_{\mathrm{b,i}} \right) dt \tag{18}$$

Drag force on each bubble:

$$F_{\mathrm{D,i}} = \frac{18\mu}{\rho_{\mathrm{b}} d^2{}_{\mathrm{b,i}}} \frac{C_{\mathrm{D,i}} Re_{\mathrm{i}}}{24} \tag{19}$$

Particle Reynold's number:

$$Re_{\mathrm{i}} = \frac{\rho d_{\mathrm{b,i}} \left| \underline{u} - \underline{u}_{\mathrm{b,i}} \right|}{\mu} \tag{20}$$

where, ς and r are integers between 0 and 1 spread evenly, $\underline{e}_{\mathrm{R}}$ represents unit vector in a random direction, C_{L} represents an empirical which equals 0.15, $\underline{x}_{\mathrm{b,i}}$, $\underline{u'}_{\mathrm{b,i}}$, ρ , $d_{\mathrm{b,i}}$, and the subscript i, are the position, fluctuation velocity, density, and diameter of each bubble [31].

Drag co-efficient:

$$C_{\mathrm{D}} = \frac{24}{Re} (1 + ARe^{B}) + \frac{C}{1 + \frac{D}{Re}} \tag{21}$$

Drag parameters A, B, C and D, for the particles, are set as non-spherical, a particle sphericity $\emptyset$ accounts for shape of particle, with S, taking particle surface area into consideration and s, representing sphere surface area having same volume as particle [32].

$$\emptyset = \frac{s}{S} \tag{22}$$

3.1.3 Simulation Approach

By resolving the continuity and unsteady Reynolds-averaged Navier-Stokes equations using local mean variables and taking into account the slip velocities between the phases, a three-dimensional multiphase flow field may be derived. The primary and secondary phases of the multi-fluid model are solved by different governing equations in Eulerian coordinate. Mass, energy, and momentum conservation equations are solved, and phase interactions are modeled to suit sharp and dispersed interface regimes [7]. Inert gas bubbles are modeled in the computational domain as discrete second-phase particles, standard k-epsilon model is activated, and the eulerian multiphase model is applied for the strong coupling effect between the continuous and dispersed phases. The fluctuation velocity is maintained for the subsequent random eddy lifespan in the random walk model, which takes into account the effects of turbulence on the trajectories [31]. Since the drag and buoyancy forces between each bubble and flow field are calculated for each time step, the flow and bubble trajectory equations are coupled.

3.1.4 Assumptions

At a temperature of 1892K, the molten metal is considered to be isothermal and slag, argon, and liquid steel are considered incompressible Newtonian fluids. The slag and steel do not interact chemically during the simulation, and coalescence and breakup of bubbles are taken into account. The walls are assigned no-slip while gravity is taken into account along the y-axis.

3.2 Point Injection Model

3.2.1 Simulation approach

ANSYS Fluent CFD software was coupled with complex user-defined functions (UDF) for particle dissolution simulation. Injection into the steel is modeled to occur once and consistently for a defined period. The movement of the virtual fluid mass is tracked since the particles are identified as computation points moving with the stream at the injection point. Considerations are made for materials of different properties, and to model their behaviors within the melt, these particles have to be turned into species and carried by the momentum of the steel. The movement of the particles is identified by the discrete phase model (DPM) tracking coupled with it until they get a defined

residence time. Considering the displacement around the particle, time it takes for the formed shell to melt, allowing the alloy particles to diffuse within the melt and eventually dissolve when introduced into the bath, is defined as its "critical time t_c" within the UDF.

3.2.2 Model Details

In the UDF code, the total mass of the particles is defined in conjunction with the time it will take for the injection to complete. The total mass within each parcel records the multiplication of the number of particles in the parcel and the mass of every particle. Immediately after t_c, the mass is released into the bath and moves through the primary phase as source terms, and the particles are deleted.

3.2.3 Governing equations

The shell period phenomenon, mathematically developed by Zhang and Oeters, is depicted in the UDF file built for the simulation process taking into account the melt's solidification temperature, the alloy particle's initial temperature, and temperature of melt [16].

$$t_1 = \frac{C_p \rho R}{\pi h} \frac{T_S - T_O}{T_M - T_S} \tag{23}$$

C_p represents specific heat capacity, ρ represents alloy density, and R radius of alloy.

From Aoki et al. [31], the heat transfer coefficient h, at the surface of the ferroalloy particle is estimated from Reynold's number Re, and Prandtl number Pr using Whitaker's Nusselt number correlation [33].

$$Re_i = \frac{\rho d_A \left| \underline{u} - \underline{u}_A \right|}{\mu} \tag{24}$$

$$\mathrm{Pr} = \frac{C_p M \mu}{k M} \tag{14}$$

$$(Nu - 2) = \left(0.4 Re^{\frac{1}{2}} + 0.06 Re^{\frac{2}{3}} \right) Pr^{0.4} \tag{26}$$

$$h = \frac{Nuk_{\mathrm{M}}}{d_{\mathrm{A}}} \tag{27}$$

During their dissolution into a mass source of liquid solute, the inert gas particles are assigned spherical drag characteristics. Assuming that the particles are spherical, the DPM is utilized to predict the motion of the alloy. Integrating the particle velocity equation yields the ferroalloy particles' trajectories from the estimated velocity field [25]. The multiphase flow model equations for force balance and drag on each bubble, bubble trajectories, and Reynolds number alloy particles are used to compute species transport [31]. The time it takes for the mixture to homogenize completely is known as the "mixing time."

Drag law:

$$C_{\mathrm{D}} = a_1 + \frac{a_2}{Re} + \frac{a_3}{Re^2} \tag{28}$$

where a_1, a_2, a_3 are constants that apply over ranges of Re given by Morsi and Alexander [30].
This model is calculated in FLUENT, where a User Defined Function (UDF) is compiled for the mathematical application of the shell period.
From Fig. 3.1, the step by step alloy process is illustrated and the species transport model is activated to describe the alloy mixing after shell melting.

$$\frac{\partial}{\partial t}(\rho \mathrm{C}) + \nabla \cdot (\rho u \mathrm{C}) = \nabla \cdot \left(\rho D_{\mathrm{M}} + \frac{\mu_{\mathrm{t}}}{Sc_{\mathrm{t}}}\right) \nabla C \tag{15}$$

where C is the local mass fraction of the alloy element; D_M is the diffusion coefficient of the alloy element ($m^2\ s^{-1}$); and Sc_t is the turbulent Schmidt number defined as 0.7 [25].

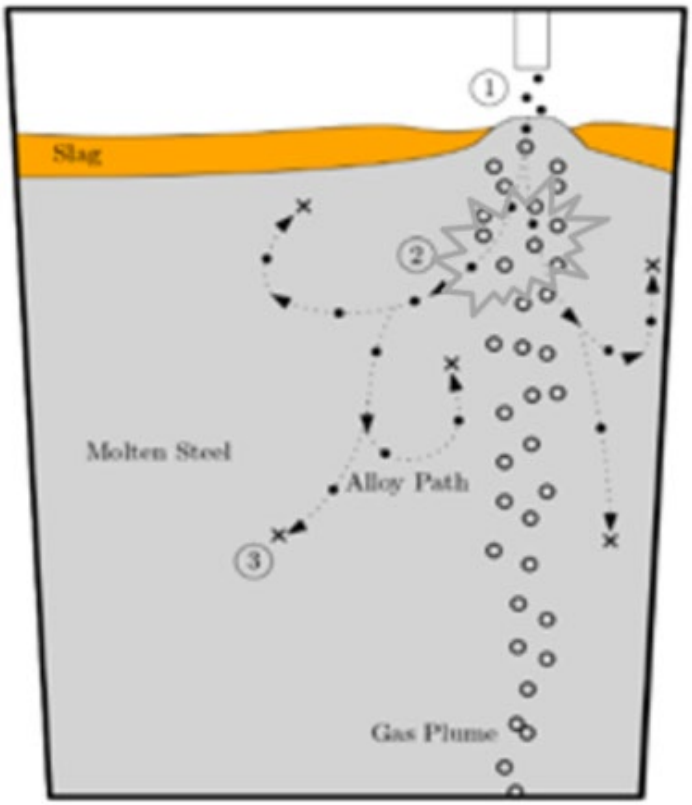

Figure 3.1. Injection Process: (1) alloy entrance (2) shell formation and melting (3) dissolution.

4. COMPUTATIONAL DETAILS AND BOUNDARY CONDITIONS

4.1 Flow Field

4.1.1 Geometry and Mesh

The three-dimensional domain depicted in Fig. 4.1 features of the LMF geometry comprising three zones: air, slag, and steel, with two porous plugs of diameter 0.104m at the bottom. The steel height and slag thicknesses are 3.23m and 0.147m, respectively. Small cell sizes are utilized to capture flow phenomena, resulting in a long computational time.

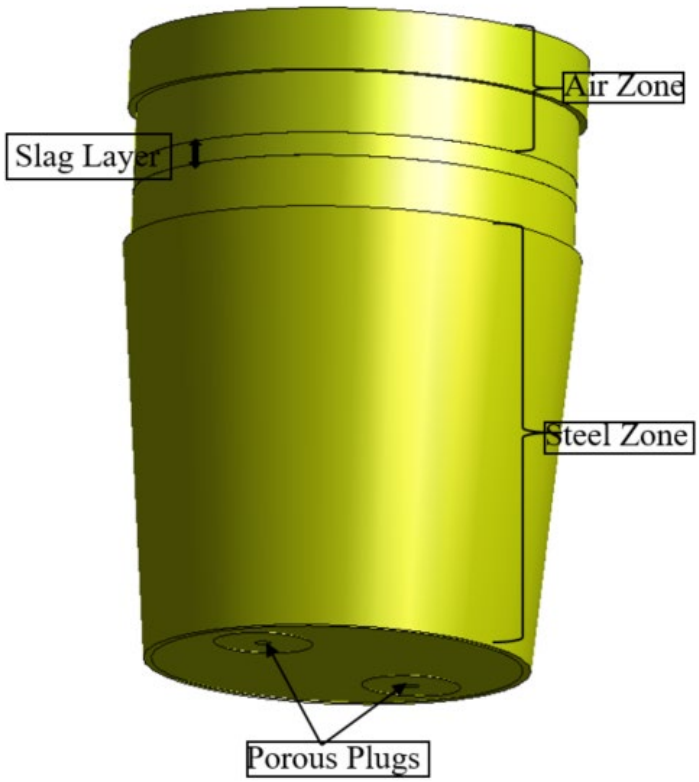

Figure 4.1. LMF Geometry.

The grid in Fig. 4.2, created for the ladle geometry is a structured hexahedral, with a fine cell count of approximately 1.2 million having a maximum skewness of 0.6 and a minimum orthagonal quality of 0.4. This was then replicated twice, with lesser cell counts of 0.7 million and 0.4 million, to study its effect on results obtained from the flow field and ensure reasonable differesnce in the resolution. Equal and constant inert gas flow rates of 0.85 m^3/min are used for each plug, with a

mean bubble diameter of 0.015m injected. Transient formulation of second-order implicit is utilized.

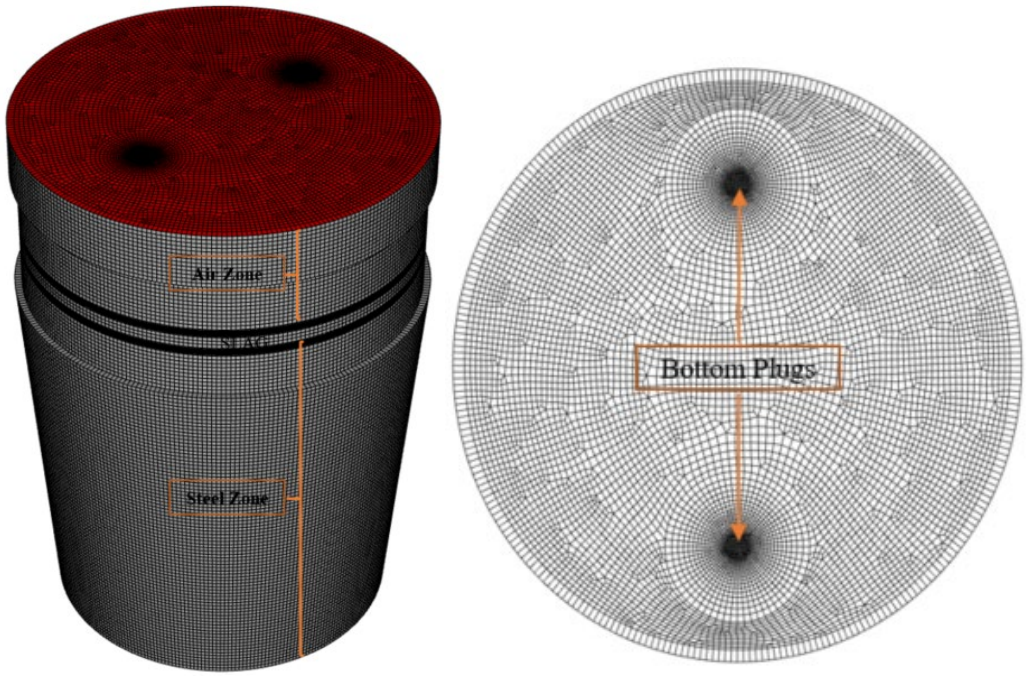

Figure 4.1. Ladle mesh.

Table 4.1. shows parameters utilized for the computation of mesh sensitivity and parametric studies on the effects of argon flow rates, asymmetric flow, and the number of ladle plugs on stirring intensity. These conditions greatly influence stirring intensity, flow pattern, or slag eye formation.

Table 4.1. Physical properties of argon and steel melt.

Property	**Value**	**Unit**
Liquid steel viscosity	0.0062	Pa.s
Steel surface tension	1.4	N/m
Melt density	6795	kg/m^3
Argon density	1.6	kg/m^3
Slag density	2785.96	kg/m^3

The study replicated on three different grids evaluates the mass-averaged flow velocity of all three meshes on planes defined within the steel zone as in Fig. 4.3, characterized by heights. Planes 1, 2, and 3 possess heights of 0.22m, 1.22m, and 2.22m, respectively.

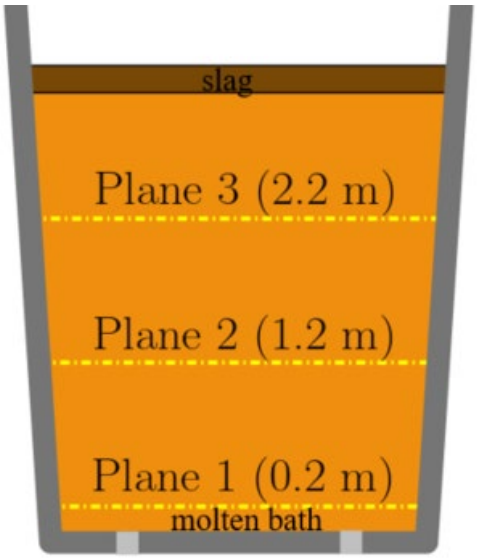

Figure 4.2. Plane Positions.

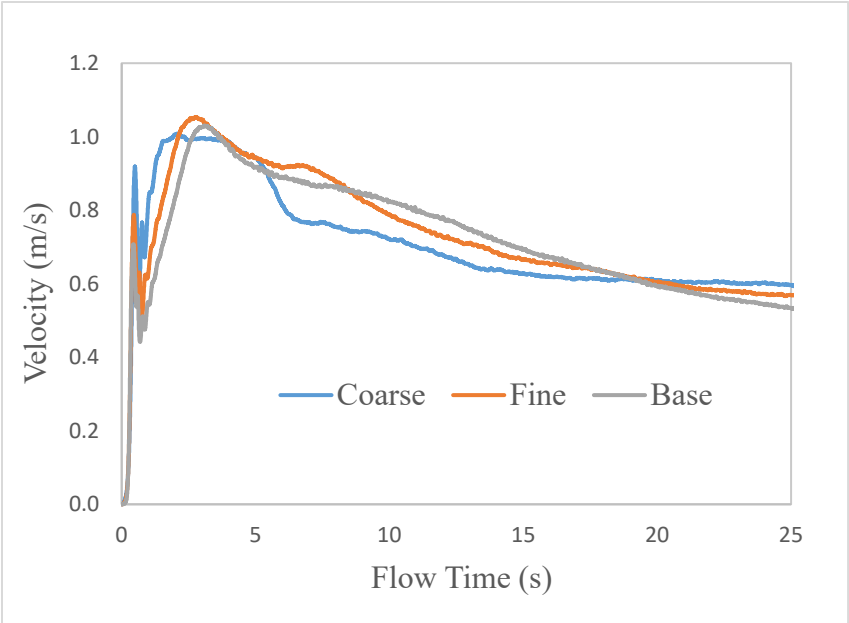

(a) Plane 1

Figure 4.3. Average flow velocities on different planes.

Figure 4.3 continued

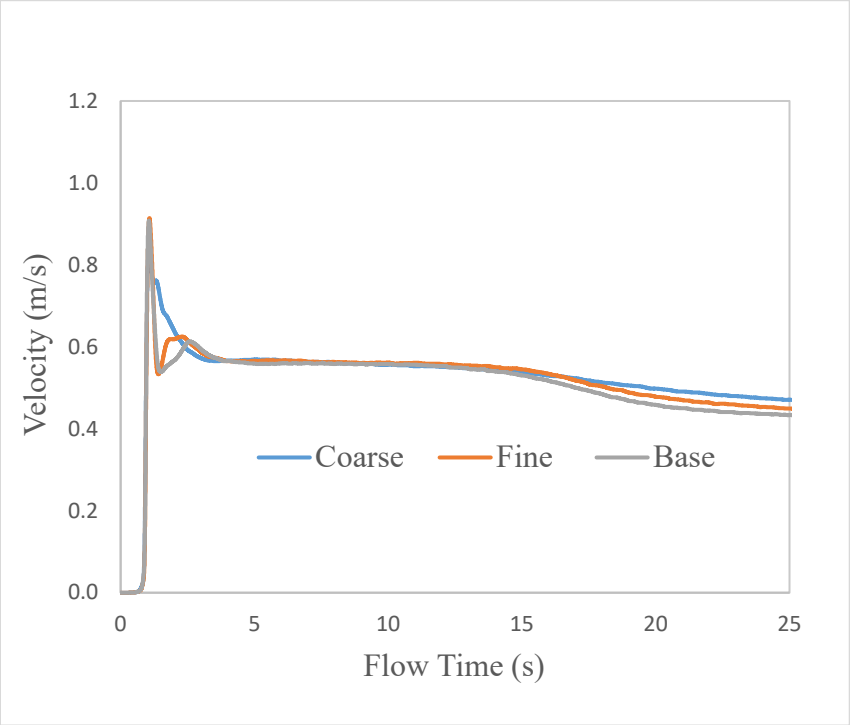

(b) Plane 2

(c)

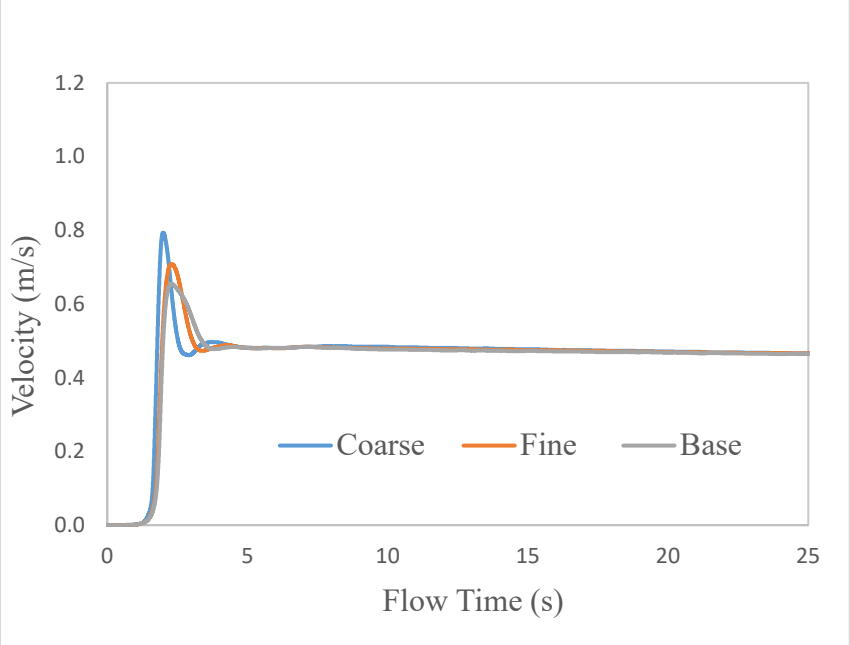

(c) Plane 3

Comparison of mass-averaged flow velocity on each plane for all meshes follow similar trend as can be seen on the plots in Fig. 4.4. However, the base case utilized for further investigation was selected as a result of its finer mesh and properties such as count for more accurate calculation.

4.2 Alloy Mixing

4.2.1 Mixing

The overall simulation is carried out in a two-step procedure, and mixing is done as soon as flow field attains a quasi-steady state. Before addition, flow and turbulence calculations are deactivated, and particles can either be added through bulk additions, powder injection or wire feeding [34]. As the particles are diffused into steel, homogeneity is tracked, and a comparison is made with industry data to ascertain the alloy concentrations after an amount of time. This investigation focuses on bulk additions as it is widely practiced and known to be cost-effective. Fig. 4.5 illustrates the trend of particle concentration during mixing to till mixture attains a range of homogeneity.

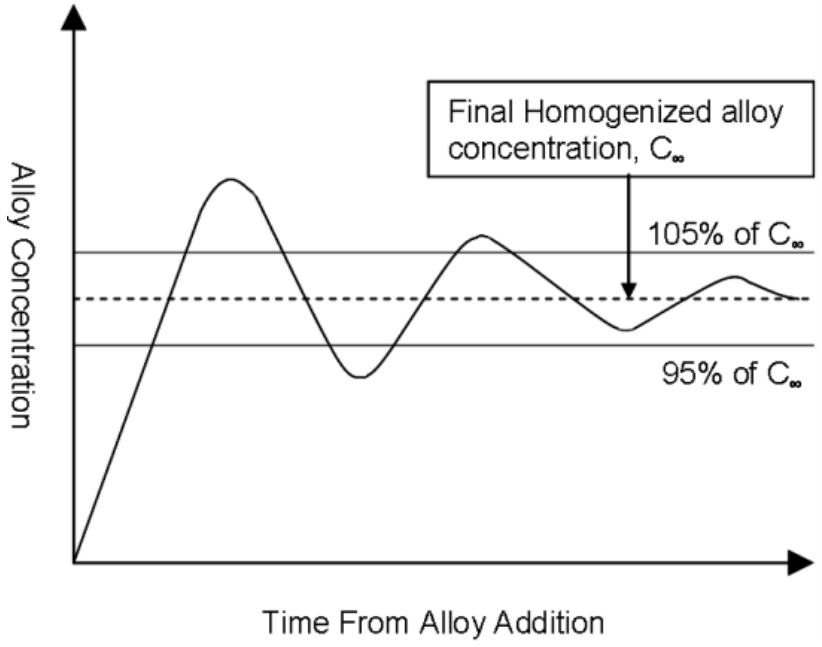

Figure 4.4. Concentration of Alloy versus Time [13].

Table 4.2. Material Properties for Mixing.

Heat capacity of molten steel	820 J/kg.K
Heat capacity of copper	390 J/kg.K
Thermal conductivity of steel	40.3 J/m.s.K
Copper density	8960 kg/m^3
Liquidus temperature of steel	1805 K
Diffusion co-efficient of alloy in liquid steel	6.4 x 10^{-9} m^2/s

The injection location is mapped within the steel region at a calculated distance slightly below the slag eye. The Air zone is set to a specified shear condition, with the DPM boundary condition set to escape. The walls of the ladle are kept at no-slip condition and locations within cells are marked across the steel bulk for accurate analysis of mixing time as seen in Fig. 4.6.

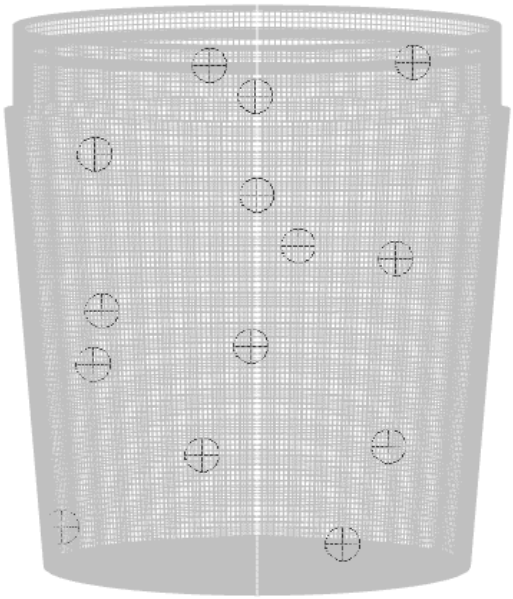

Figure 4.5. Monitoring Points within steel zone.

5. RESULTS AND DISCUSSION

5.1 CFD MODEL VALIDATION WITH PLANT DATA

The validation of this work relies on properties obtained from Nucor Steel using their generic ladle design dimensions. The domain utilized as the base case for particle injection simulation was 1.2 million computing cells. First, each porous plug is turned up to a maximum flow rate of 0.85 m3/min during gas stirring to ease the charging of the alloys, which come in irregularly sized pellets of 0.0064m in diameter, added over 30 seconds. Then, 250 lbs of copper are injected, and concentrations are measured each minute after addition to determining the amount recovered. The table and graph below compare CFD model data against plant homogeneity test measurements.

A single injection is defined in discrete phase at a constant rate of 3.78 kg/s and a downward velocity of 6 m/s along the y-axis corresponding to a vertical freefall velocity. The residence time of the shell is defined as a constant within the compiled UDF, and the initial temperature of steel at the start of the homogeneity test is 1892K. As each measurement is taken, there is a gradual reduction. The least temperature recorded is at 1876K, and the liquidus temperature is taken at 1805K. The record of copper evolution over time is stated in the table below. Samples are taken 7 inches below the top of the ladle from an established region within the axis of one of the CFD plugs, corresponding to the plant location as shown in Fig. 5.1.

Table 5.1. Recovered Copper Concentrations.

Temperature (K)	Time (s)	Plant (wt. %)	CFD (wt. %)	%Δ
1892	0	0.2485	0.2485	0
1892	60	0.342	0.3411	0.3
1885	120	0.345	0.3229	6.4
1881	201	0.362	0.3145	13.1
1876	240	0.367	0.3109	15.3
1880	300	0.375	0.3085	17.7
1878	360	0.367	0.3065	16.5

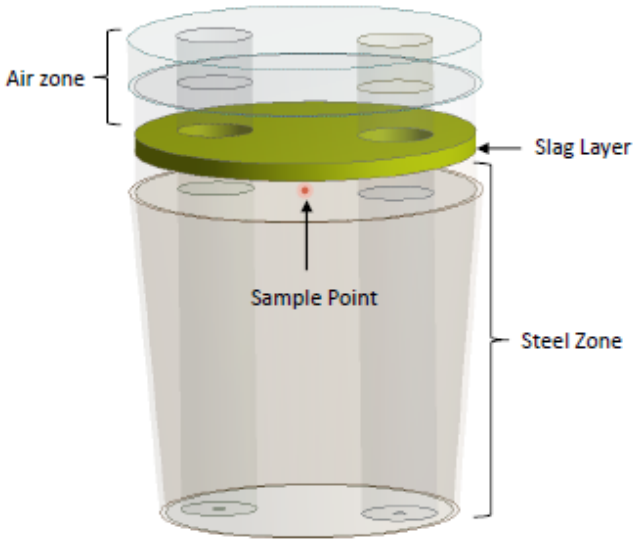

Figure 5.1. Sample location within steel zone.

5.2 Flow Field

5.2.1 Flow Pattern Analysis

At the center plane, a region of recirculation is revealed between the plumes, alongside dead zones at the bottom corners of the ladle furnace. The recirculation zone affects how fast and to what extent mixing occurs, while the dead zones may indicate local concentration fluctuations. Further analysis at the vortex core region, colored by velocity, reveals a gradient of energy-concentrated areas along the metal-slag interface. The local gradient allows mixing, and the strain field expands the mixing region between the plumes. In addition, the flow intensity during the gas-liquid interaction by the plume creates slag eyes of diameter 0.66m above plugs 1 and 2. Relative velocity $\left|\underline{u} - \underline{u}_{\mathrm{A}}\right|$, obtained from computation equals 0.44m/s.

5.3 Dissolution and Mixing

5.3.1 Particle Behavior

The injection point is marked at 0.43m below the slag eye, where particle velocity trajectory is tracked location-based. No significant displacement is recorded at the emission point except the existing flow field plume momentum, which offsets the particle velocity by forcibly reducing it,

causing them to spread outwards and then slowly trail downwards before dissolving into the melt after the assigned critical time tc has elapsed as depicted in Fig. 5.2. After dissolution, particles remain within the continuous phase while the simulation is further run until mixture homogeneity is obtained. Mixing time values for each simulation are different at 95% homogenization, as this is confirmed to depend on the gas flow rate. Figure 5.3 shows that the particles are released from the single injection point. It also reveals the plume zone and the slag isosurface.

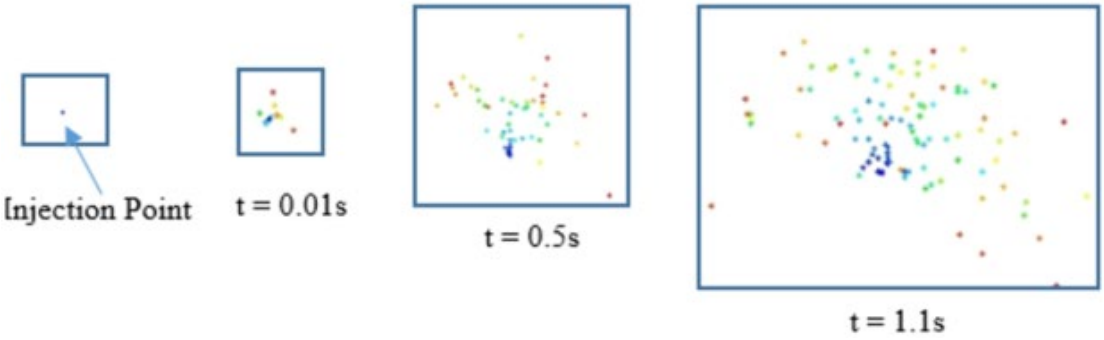

Figure 5.2. Particle behavior at injection points.

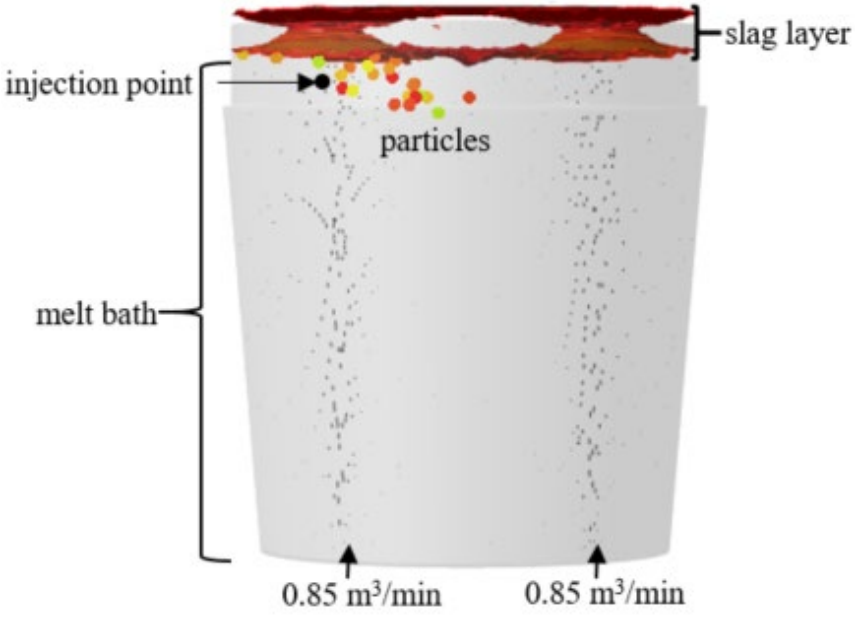

Figure 5.3. Particle release using point injection.

Copper Dissolution

The time distribution of the particle release, shell formation and species dissolution can be seen in the mass fraction contours in Fig. 5.4. Investigation of the discrete phase velocity magnitude of the particles as they enter the liquid steel reveals a massive reduction. Since copper is denser than steel, the particles drop directly into the bath, gradually accumulating towards the center even as the injection occurs at the left plume. Though the initial speed is reduced due to steel movement and, of course existing momentum of the plume, it stays constant at approximately 0.8m/s for the first 15s of addition. After that, more fluctuations are recorded, with the lowest speed of 0.11m/s observed at 75s.

From the injection point, the particles accumulate between the plumes and a shell of mass forms around the perimeter of the copper particles. After the critical time of 1.14s, it melts, leaving the alloy to slowly dissolve and diffuse across the steel bulk, sinking towards the bottom. Approximately 14.2 minutes is the total time for the mixture to homogenize.

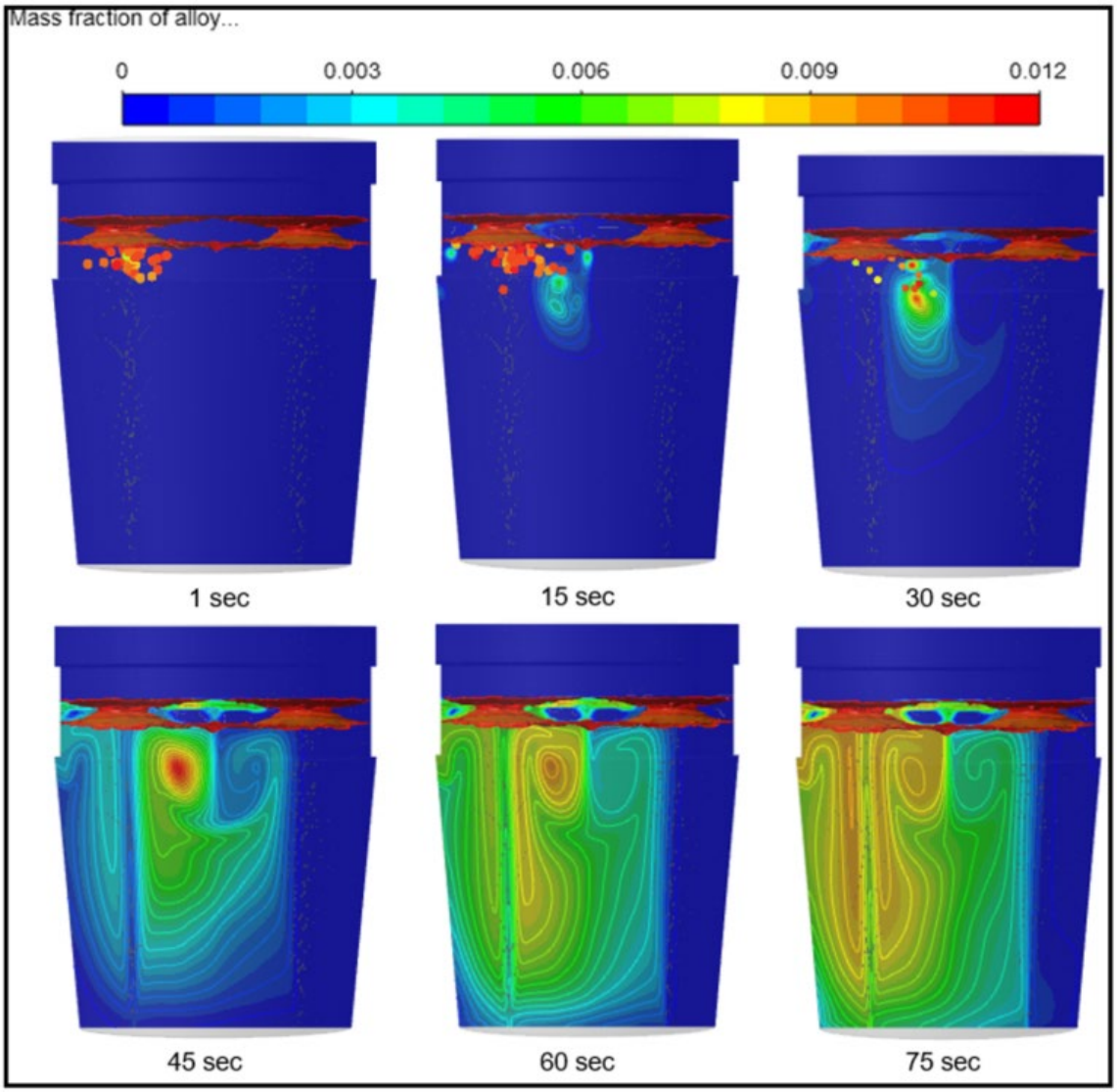

Figure 5.4. Mixing behavior of copper for 1.70 m^3/min total flow rate.

Further parametric simulations are carried out utilizing an asymmetric flow field and a single plug ladle design to show the impact of argon flow rate on alloy dissolving behavior. Also, two primary microalloying elements of the same size were evaluated to understand the influence of alloy properties better.

5.3.2 Comparison using an Asymmetric Flow Field

Computation was carried out using different gas flow rates to investigate the flow structure's intensity and influence on alloy dissolution and mixing time. A total of 1.13 m^3/min gas flow rate was stirred into the dual plug ladle, with one plug at 0.71 m^3/min and the other at 0.42 m^3/min. Relative velocity obtained equals 0.45m/s, and reduced spout eye area is noticed in the slag when compared against the base flow field since both possess dissimilar stirring power. The cross-sectional area of plume has a significant impact on circulating flow, as shown by the vector contours of velocity magnitude in Fig. 5.5. This change in the flow pattern inside the ladle is noteworthy.

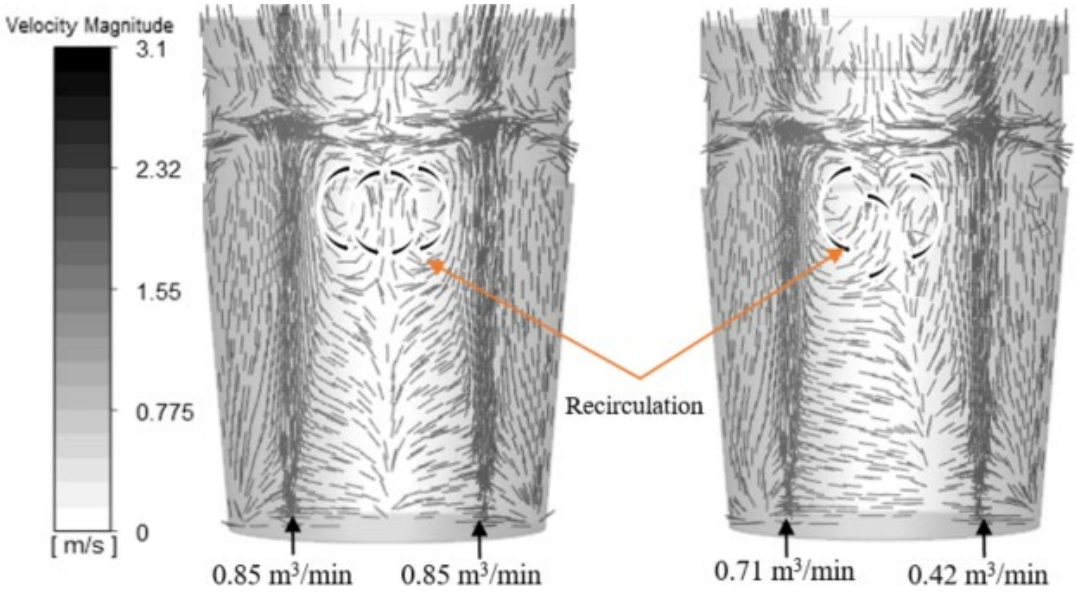

Figure 5.5. Vector contour of flow field.

For the asymmetric flow field, most of the recirculation seems to be pushed towards the higher flow rate, unlike the baseline flow, which shows centered recirculation regions between the plumes.

As recirculation drives for faster mixing, the same copper mass is injected into the flow field to observe the changes as the particles diffuse. During injection, the DPM particle velocity magnitude in this varied flow massively fluctuates, as shown in the particle tracks color bar in Fig. 5.6. The

same behavior of the copper particles from the base case is seen; however, the cluster of mass formed in the melt is closer to the higher flow rate plume, exactly where the region of recirculation was noticed in the flow field prior to subsequent melting. The time it takes for the steel shell to melt, allowing the copper particles to dissolve, is 1.13s.

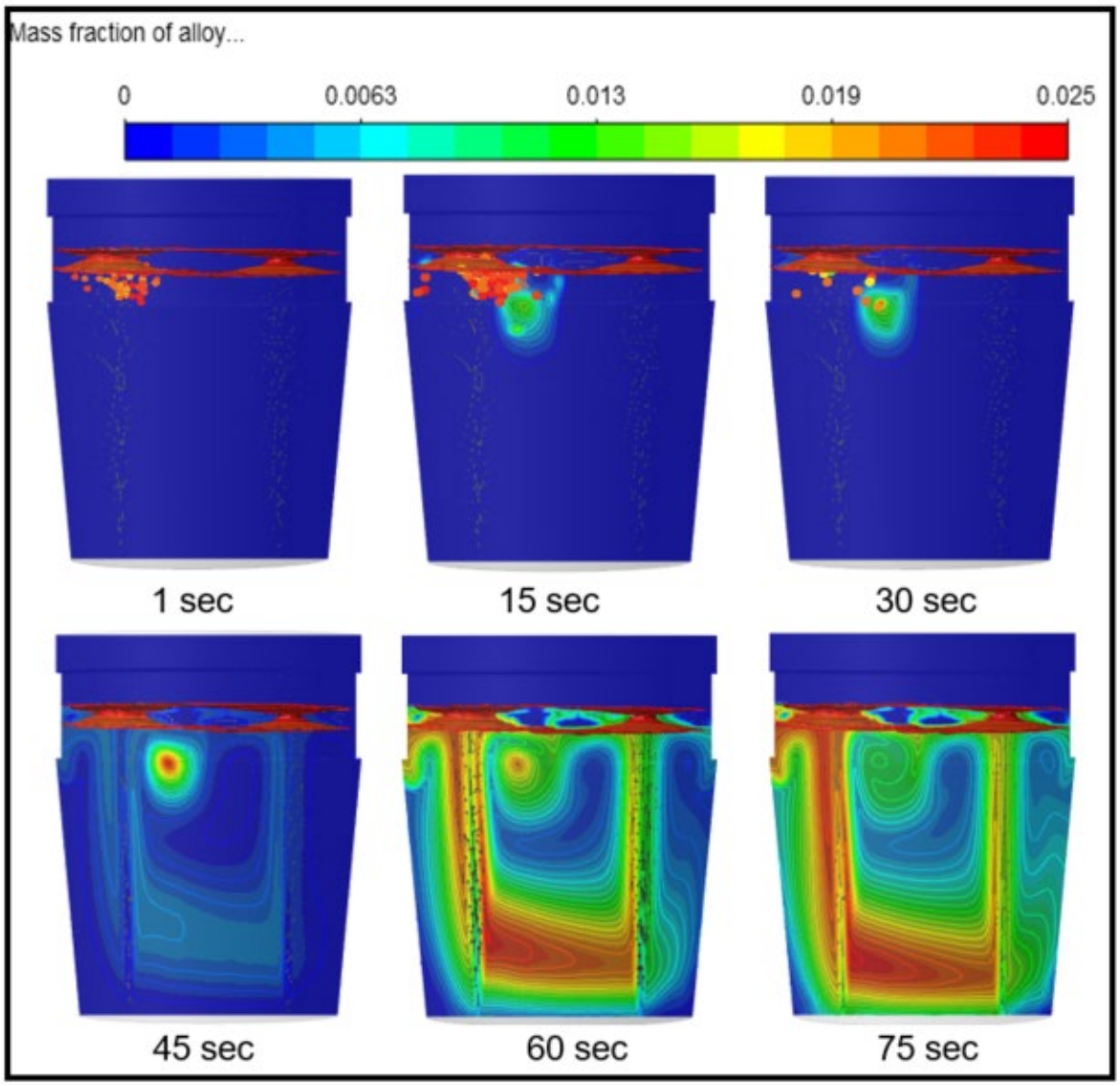

Figure 5.6. Mixing behavior of copper for 1.13 m^3/min total flow rate.

At 60secs of mixing, the mass fraction of copper species can be seen to have almost totally diffused across the molten bath. At specified homogeneity, the total mixing time recorded is approximately 5.6 minutes.

5.3.3 Single and Dual Plug Mixing Comparison

Fig. 5.7. shows plot of flow velocity comparison for single and dual plug ladles from the initial flow field at a surface plane created 1m below the steel-slag interface and relative velocity obtained from computation, equals 0.52 m/s. Due to impingement on the slag caused by plume intensity at flow rate of 0.85 m^3/min, the diameter of the spout eye created is approximately 19 inches and flow recirculation is noticed near the plume and close to the walls.

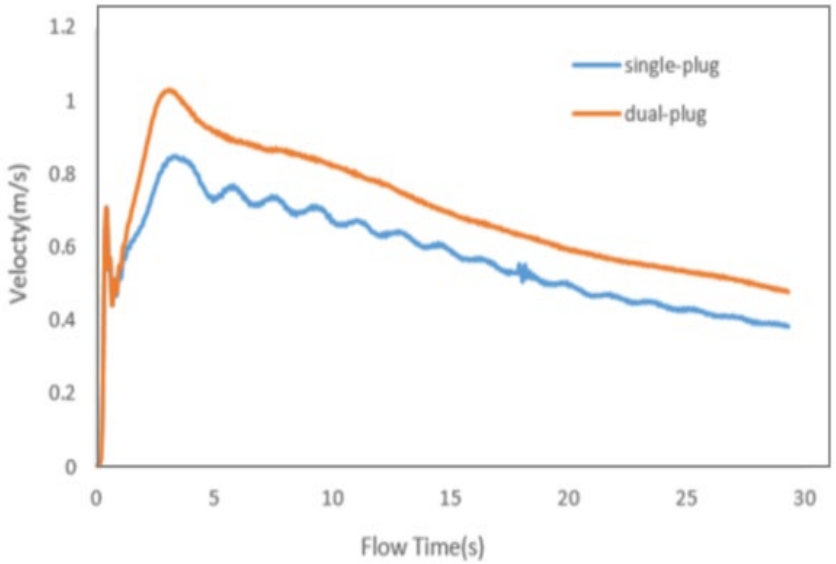

Figure 5.7. Flow velocities for single and dual plug ladles.

The same particle injection process is carried out here. From the contours, the copper mass can be seen to move towards the center even though the injection occurs within one plume. When the steel shell melts after 1.05s, there seems to be a slow diffusion of the particles as they are gradually distributed downwards.

In all time variations of the contour plots in Fig. 5.8, there seem to be high concentrations of the copper mass fraction closer to the plume region, even as dissolution is occurring. However, the total time of tracked homogeneity recorded is approximately 5.6 minutes.

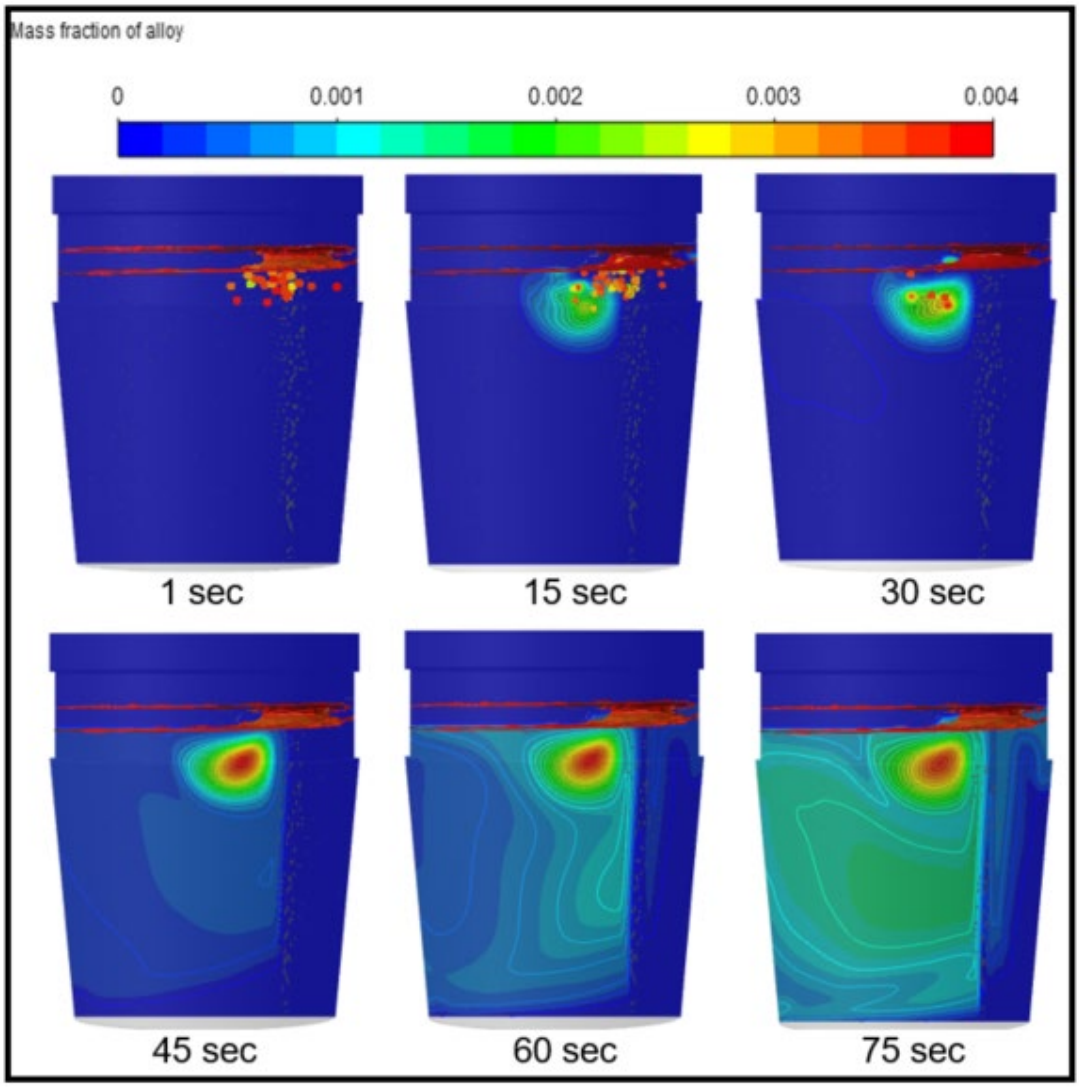

Figure 5.8. Mixing behavior of copper for 0.85m^3/min total flow rate.

5.3.4 Dissolution Behavior of Different Alloys

The microalloying elements utilized are based on their popularity in the industry and their densities compared to steel. The copper material used for plant validation is the dense of the three tested, and vanadium is the least dense. According to the requirement for good alloying practice [13], the steel shell must be melted for the particles to either resurface or reach the ladle bottom for alloys with high or low densities. Exothermic interactions between the alloy and the steel shell are not taken into consideration by the shell model specified in the UDF code. It's important to understand that the specific alloy type and its associated qualities have an impact on how the steel shell forms.

Table 5.2. Properties of Alloying Elements.

Alloy	Density (kg/m3)	Melt Temperature (°C)	Specific Heat Capacity Cp (J/g.K)	Viscosity (kg/m-s)
Copper	8960	1083	0.390	0.0021
Columbium	8570	2467	0.272	0.0045
Vanadium	6140	1890	0.502	0.0045

Each specific heat capacity and viscosity are utilized to obtain the critical time of dissolution of the shell. It is observed that within the model, the number of particles in a parcel is unique to a particular alloy, as fluent recalculates it in adjustment to updated parameters, regardless of the defined mass. Each alloy displays almost the same behavior during injection as represented in the contours of species mass fraction.

Columbium Dissolution

Columbium possesses a relatively high melting point but has the shortest shell existence time of 0.758s amongst all three micro alloying elements. The contours in Fig. 5.9 show rapid dissolution towards the ladle bottom after the shell melts. The concentration distribution is more intense and dispersed across the bath than copper, which could be attributed to its lower density. Sismanis [35] points out in his thesis that a reaction occurs at the steel shell/columbium interface for lower bath superheats, unlike in the higher bath superheats. Although the reaction is not considered in this study, he mentions that the dissolution speed of columbium increases under dynamic conditions (stirred baths). Cruz et al. [36] concur with this by adding the potential of obtaining high recovery yields of the alloy, which is demonstrated in the concentration recovery results.

During the dissolution of the alloy, mass flux is controlled by the bath temperature, and the continued agitation of the melt considerably increases this mass flux. The total time it takes the mixture to homogenize is 13.8 minutes.

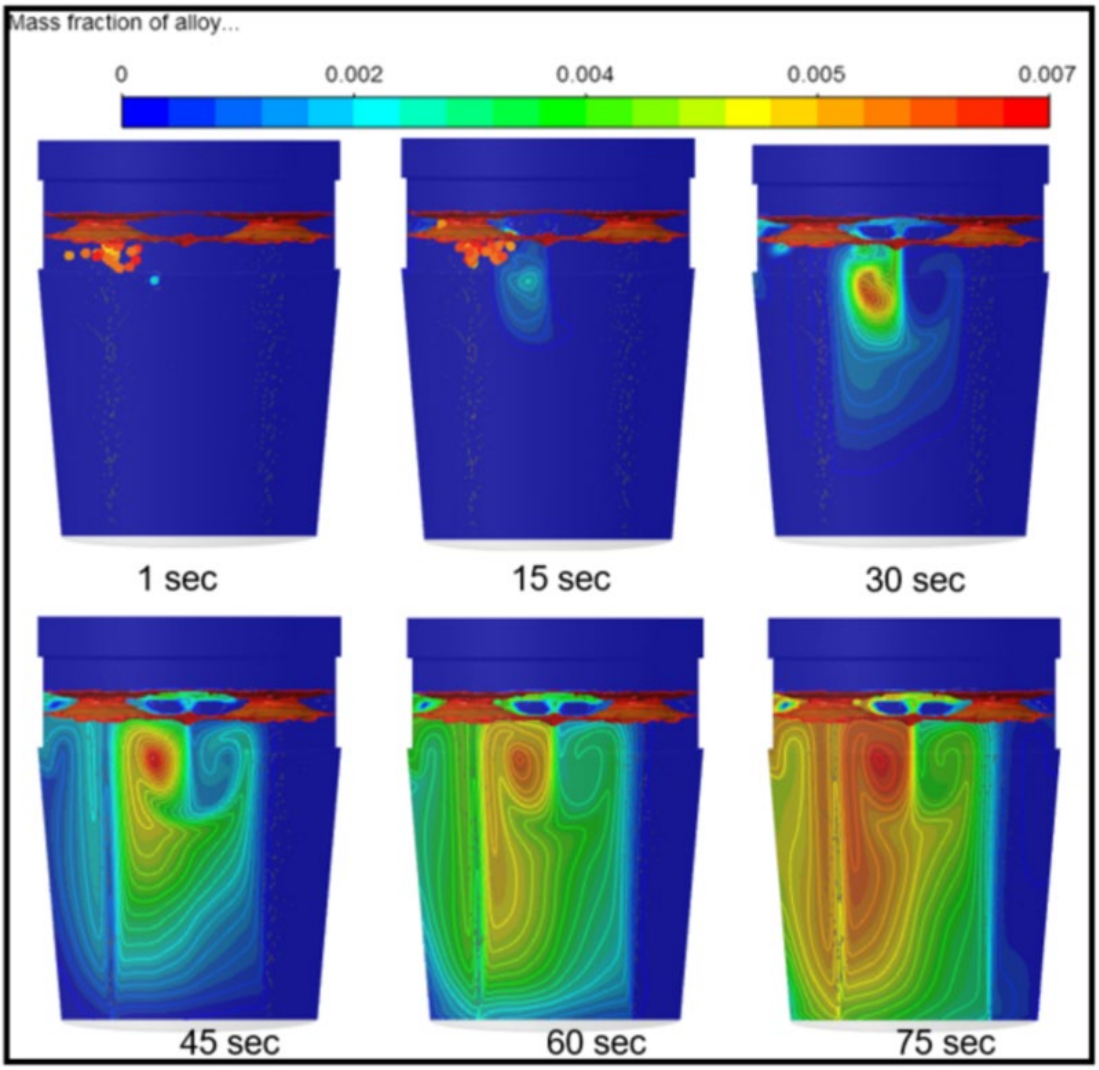

Figure 5.9. Mixing behavior of vanadium alloy for 1.7 m^3/min total flow rate.

Vanadium Dissolution

Vanadium has high solubility even at temperatures lower than its melting temperature and is less dense than steel therefore, over 90% of the addition is immersed in the bath, which lowers oxidation losses and speeds up breakdown. Again, this study does not emphasize the chemical reactions of this alloy within the molten steel. Recovery of the alloy can be very high when standard addition practices are utilized.

The calculated time for shell existence is exactly 1 second. According to mass fraction behavior seen in Fig. 5.10, the velocity magnitude of the particles is significantly reduced, and the cluster of mass is not as intense as that of the other alloys.

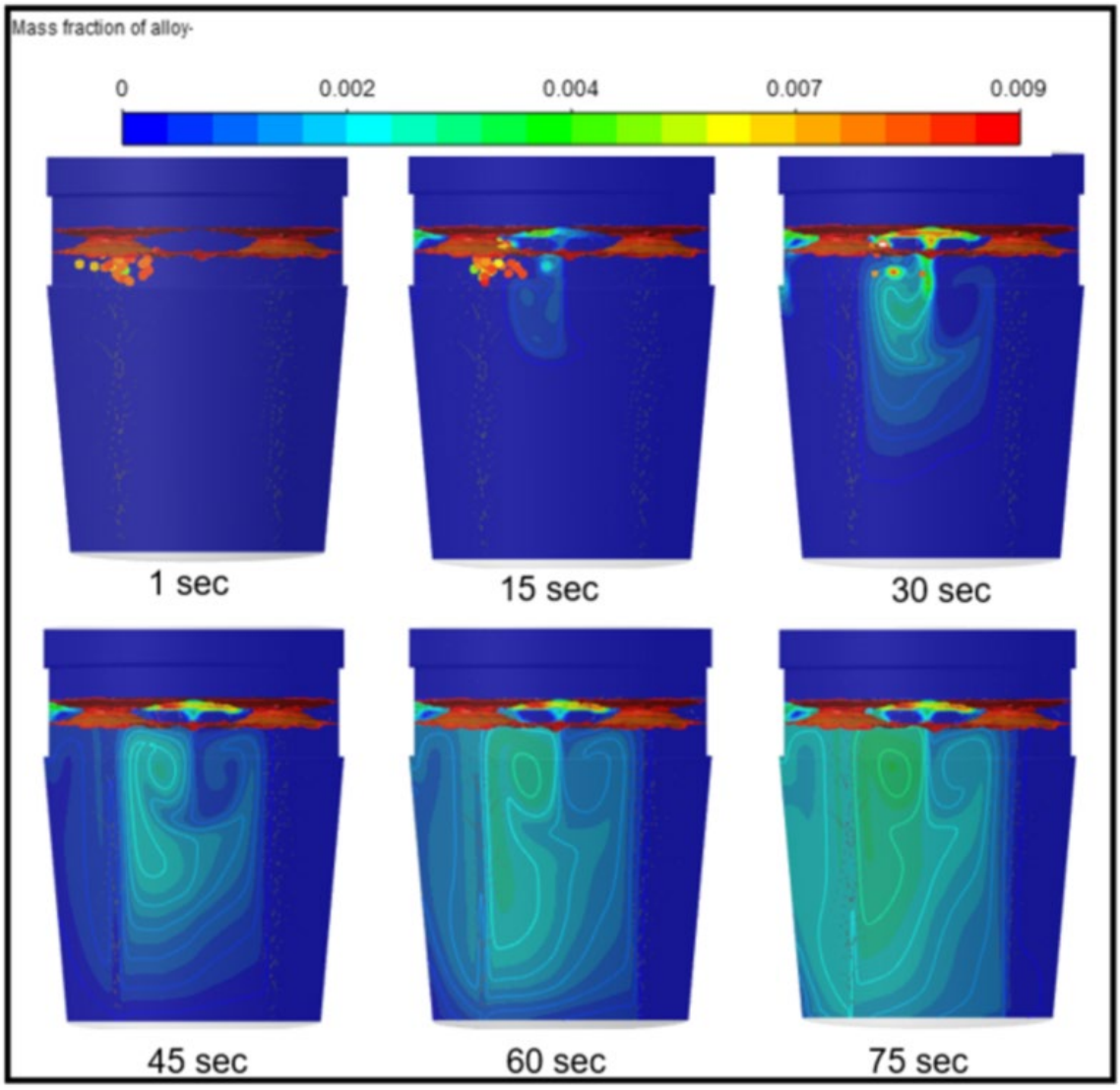

Figure 5.10. Mixing behavior of vanadium alloy for 1.7 m^3/min total flow rate.

5.3.5 Mixing

Positions relative to the alloy release location for the sampling of mixing behavior play a significant role. Determining the total mixing time when the normalized concentration reaches 95% -100% homogeneity involves taking the variance of the concentrations obtained from the already established monitoring points. Concentration at monitoring points versus the mixing time plot in Fig. 5.11 reveals the variation in time for each computed case to obtain 95% homogeneity. There may be time overprediction if some sites are situated within dead zones or in circumstances where the time is impacted by the superheat since mixing time depends on mean ladle radius,

gravity, depth of melt and gas flow rate of addition. Aoki et al. [31] relates explicitly the dependence of mixing time on the flow field.

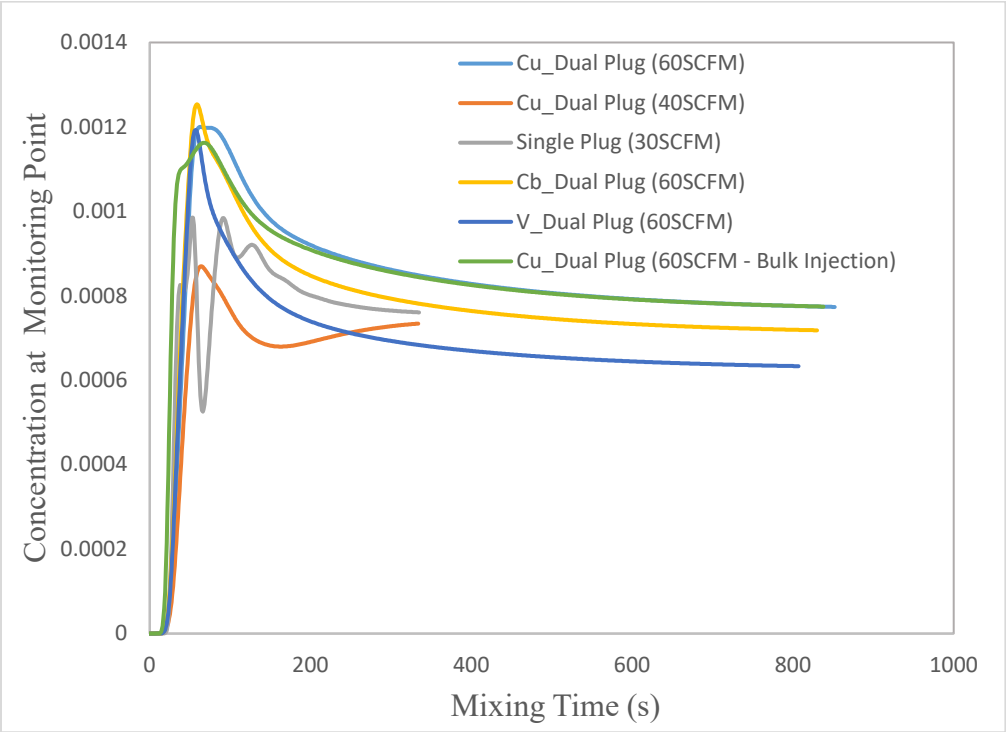

Figure 5.11. Concentration profile from same monitoring point stopping at respective mixing times.

5.3.6 Alloy Recovery

Variations in the concentration measurements, possibly caused by extensive turbulent fluctuations in the liquid steel, result in differed circulation behavior at the point of alloy addition.

The exact sample location from the baseline was assigned to all cases, and concentrations obtained in each simulation were again compared against plant data. The temperature of the melt fluctuates as the amount of copper recovered at every minute reduces with an increase in time.

Table 5.3. Recovered Copper Concentrations on Parametric Studies.

Temperature (K)	Time (s)	Plant (wt. %)	Dual Plug (1.7 m^3/min) (wt. %)	Dual Plug (1.13 m^3/min) (wt. %)	Single Plug (0.85m^3/min) (wt. %)
1892	60	0.342	0.3411	0.2930	0.3240
1885	120	0.345	0.3229	0.2864	0.3213
1881	201	0.362	0.3145	0.2812	0.3161
1876	240	0.367	0.3109	0.2809	0.3131
1880	300	0.375	0.3085	0.2812	0.3122
1878	360	0.367	0.3065	0.2813	0.3120

The recovery of copper in all three parametric studies is summarized and compared against plant data in Table 5.3. Temperature of the melt fluctuates as the amount of copper recovered at every minute reduces with increase in time as with the validated case. The results support that difference in circulation behaviors due to changes in number of plugs or reduced flow rate during stirring impacts flow turbulence in the ladle. This occurrence introduces percentage differences when concentrations at the same location are taken.

Concentrations of each alloy are collated from exact sample point location as that of the plant. Table. 5.4 and Fig. 5.12 show similar trend of reduced concentration as time of mixing increases for all three alloys evaluated showing the consistency of the model in defining the characteristic behavior of particles. Copper was the most concentrated while vanadium had the least when compared to all three, which could be attributed to some of the particles attaching to the slag as a result of the initial flotation.

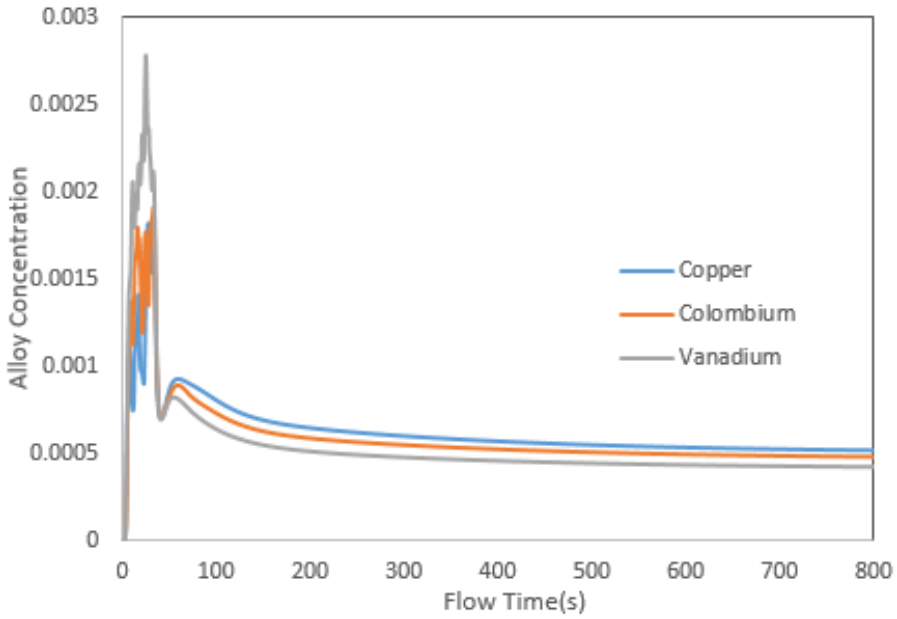

Figure 5.12. Alloy concentration profile at defined sample points.

Table 5.4. Recovered Alloy Concentration for all Microalloying Elements.

Temperature (K)	Time (s)	Copper (wt. %)	Columbium (wt. %)	Vanadium (wt. %)
1892	60	0.3411	0.3372	0.3290
1885	120	0.3229	0.3158	0.3074
1881	201	0.3145	0.3083	0.3007
1876	240	0.3109	0.3052	0.2979
1880	300	0.3085	0.3032	0.2962
1878	360	0.3065	0.3016	0.2949

5.3.7 Bulk Injection

While observing the point injection model's addition process, it is important to determine whether a single point injection lasting 30 seconds has a greater or lesser impact than an array of injections that represent the alloy material striking the steel and spreading out over a larger area to more accurately mimic the practice of dumping in the industry. Utilizing the discrete phase model single injection type to create ten consecutive points directly below the slag eye, a bulk injection was conducted for 3s simultaneously from each injection point. A similar downward velocity of 6m/s was defined along the y-axis, and addition was carried out at the same rate of 3.78 kg/s.

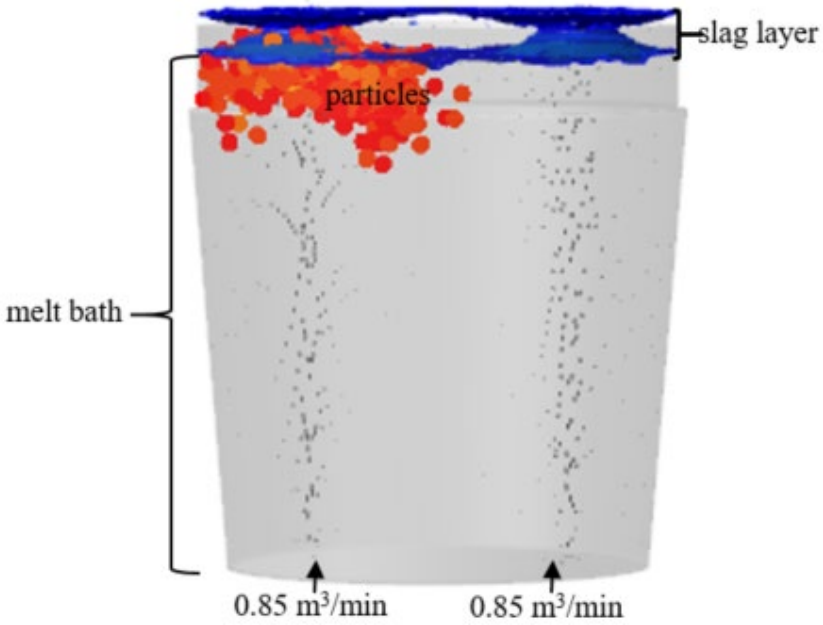

Figure 5.13. Particle release using bulk injection.

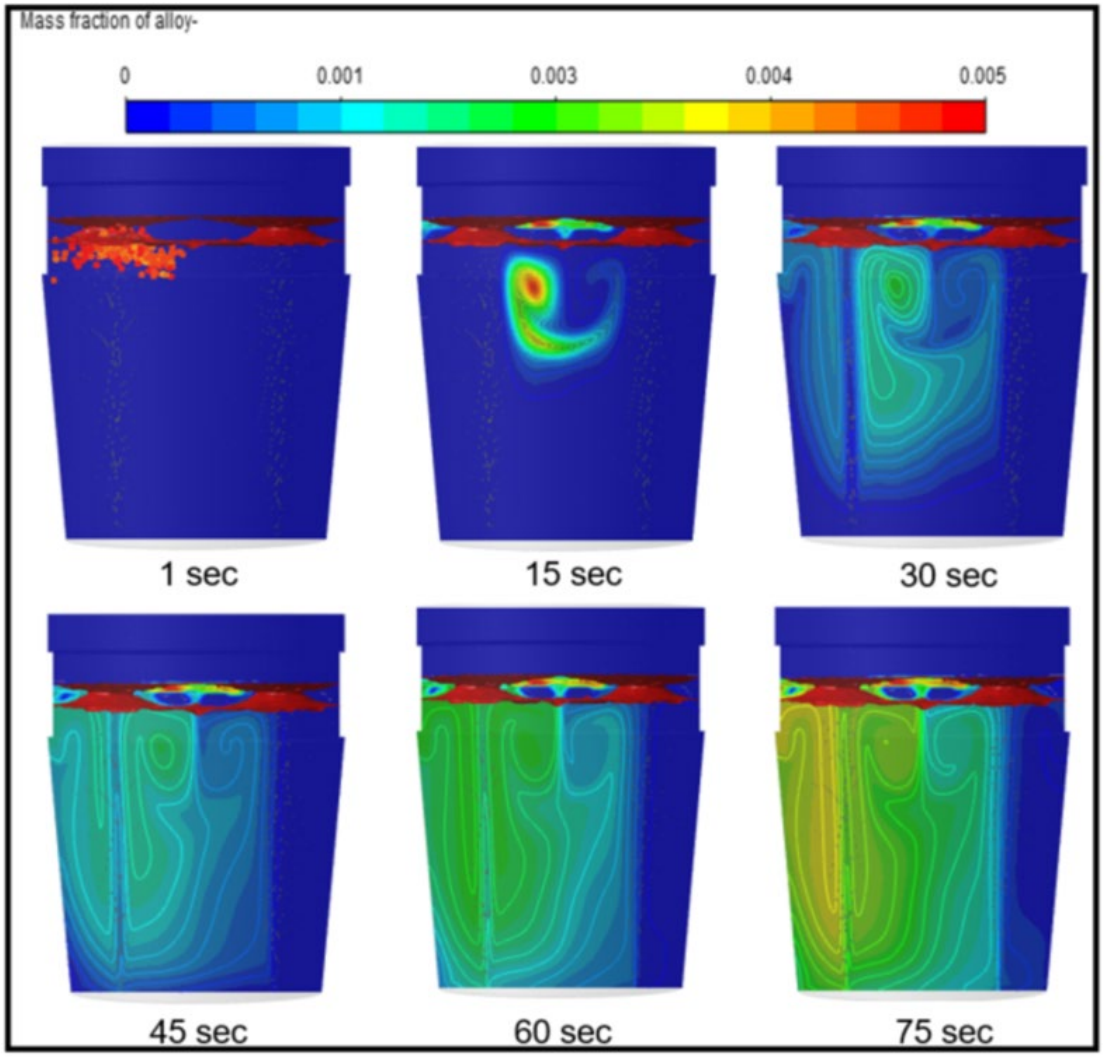

Figure 5.14. Mixing behavior of copper alloy for 1.7 m^3/min total flow rate using bulk injection model.

The steel shell existence time used is the same as the base case utilized for validation. The mass fraction contours in Fig. 5.144 shows copper particles settling further down the melt in this case because of reduced time of particle release, coupled with its dispersion to broader areas. Broader distribution across the bath as soon as the shell melts is noticed when compared to the point model.

Total mixing time at 95% mixture homogeneity is 14s which is 1.4% less than the point model; however, differences in copper concentrations obtained from both methods are almost the same according to Table 5.5.

Table 5.5. Alloy Concentration obtained from Sample Point for Point and Bulk Injection Method.

Temperature (K)	Time (s)	Plant (wt. %)	Point Injection Model (wt. %)	Bulk Injection Model (wt. %)	%Δ
1892	60	0.342	0.3411	0.3353	1.7
1885	120	0.345	0.3229	0.3196	0.01
1881	201	0.362	0.3145	0.3122	0.73
1876	240	0.367	0.3109	0.3103	0.19
1880	300	0.375	0.3085	0.3080	0.16
1878	360	0.367	0.3065	0.3062	0.1

6. CONCLUSION

Micro-alloy addition was simulated in a two-step process using a three-dimensional multiphase flow model. The dissolution behavior of these additions is analyzed by adopting the discrete phase and species transport models to predict particle motion and accurately describe the mixing process, respectively.

A recirculated region is noticed in between as the plume flows with an intensity up to the slag and floats outwards towards the ladle walls. The pattern of the flow field obtained corresponds with plant observations. High charging of dual plug ladle for gas stirring is analyzed by comparing it with lower gas flow rates in the same and single plug ladle to determine the necessity for an extremely high flow rate and invariably curb resource waste. The following can be drawn from the results;

- Mixing behaviors of Cu particles in all scenarios reveal that the process is heavily influenced by initial plume velocity generated during argon gas blowing, as the existing momentum slows the velocity at which the particles disperse from the point of injection, which can potentially over predict the mixing time.
- One thing of note is that unconventional varied flow rate gas stirring, when compared to standard same flow rates, results in shortened mixing time.
- Locations mapped across the steel bulk for monitoring the mixing plays a part in mixing time because if the majority of the points exist in dead zones, the process runs longer.

The addition of copper as a high strength low alloy for hydrogen-induced cracking suppression and corrosion resistance is further compared against columbium and vanadium. The particle behaviors of these alloys reiterate the influence of density, specific heat capacities, and melting points on the critical or residence time that must exist before dissolution starts to occur.

The bulk injection method entirely models the industry practice as noticed from the results and the decreased mixing time obtained supports the method. Recoveries of the concentration of individual alloys differ by specific percentages, which are as expected.

Table 6.1. Computed Cases.

Cases	**Flow Rates/Plug (m^3/min)**	**Initial Relative Velocity, $\left\|\underline{u} - \underline{u}_A\right\|$ (m/s)**	**Critical Time t_c, (s)**	**Mixing Time (minutes)**
Copper - Dual Plug	30	0.4407	1.14	14.2
Copper - Dual Plug	25 & 15	0.4457	1.13	5.6
Copper - Single Plug	30	0.5175	1.05	5.6
Columbium - Dual Plug	30	0.4407	0.758	13.8
Vanadium - Dual Plug	30	0.4407	1.00	13.5

In order to objectively examine the shell creation and its existence time, further research can be done in areas such as:

- Evaluation of non-isothermal model:
    - Temperature-dependent behaviors
    - Influence of super heat on mixing time
- Steel shell size analysis
- Slag-induced behaviors
- Reactions with injected alloys

REFERENCES

[1] Thyssenkrupp Steel https://www.thyssenkrupp-steel.com/en/newsroom/press-releases/investing-in-the-future-thyssenkrupp-to-build-new-ladle-furnace-in-duisburg.html Daily press, Trade press, 2016-04-21

[2] Satyendra; "Utilization Optimization of Ferroalloys during Steelmaking", 2019

[3] Liu, C.; Y. J,; Hao, L.; Han, S.; Huang, F.; "Effects of Slag Composition and Impurities of Alloys on Inclusion Transformation during Industrial Ladle Furnace Refining" Metals 2021

[4] Nasbeth, S.; Torner, K.; "Potential Methods of Measuring the Stirring Intensity during Secondary Steelmaking in the Ladle Furnace". Degree project in Technology, Stockholm, Sweden 2016.

[5] Peranandhanthan, M.; Mazumdar, D.; "Modeling of Slag Eye Area in Argon Stirred Ladles" ISIJ International Vol. 50 (2010), No. 11, pp.1622-1631

[6] Li, L.; Liu, Z.; Cao, M.; Li, B.; "Large Eddy Simulation of Bubbly Flow and Slag Layer Behavior in Ladle with Discrete Phase Model (DPM) – Volume of Fluid (VOF) Coupled Model" JOM (TMS) **67**, pages1459–1467 (2015).

[7] Li, L.; Li, X. ; Zhu, Z.; Li, B.; "Numerical Modeling of Multiphase Flow in Gas-Stirred Ladle: From a Multiscale Point of View", Powder Technology 373 (2020) 14-25

[8] Hua Tuo Metallurgy; "Ladle Argon Stirring"; https://www.sialloy.com/blog/ladle-argon-stirring.html

[9] Sano, M.; Mori, K.; "Fluid Flow and Mixing Characteristics in a Gas-Stirred Molten Metal Bath" 1983 Volume 23 Issue 2 Pages 169-175

[10] Joo. S.; Guthrie, R.I.L.; "Modeling Flows and Mixing in Steelmaking Ladles Designed for Single and Dual Plug Bubbling Operations" Metallurgical Transactions B 23, 765-778 (1992

[11] Warzecha, M.; Hutny, A.; Merder, T.; "Determinating the Power of Mixing of a Metal Bath during Processing in a Ladle Furnace"

[12] Mantripragda, V.T.; Sarkar, S.; “Slag Eye Formation in Single and Bottom Purged Industrial Steelmaking Ladles”, Canadian Metallurgical Quarterly, ISSN: 1879-1395 (Online)

[13] Webber, D.S.; “Alloy Dissolution in Argon Stirred Steel”, Doctoral Dissertation

[14] Engh, T.A.; Sigworth, G.K.; Kvithyld, A.; “Principles of Metal Refining and Recycling”, Oxford University Press

[15] T. A. Engh, Principles of Metal Refining: Mixing, Mass Transfer and Numerical Models

[16] Zhang, L.; Oeters, F.; “Mathematical Modeling of Alloy Melting in Steel Melts, Steel Research”, Vol. 70, Issue 4+5, 1999

[17] Argyropoulos, S. A.; “The Solution Rate and Recovery of Ferroalloys”

[18] Deeley, P.; Kundig, K.J.A.; Spendelow, H.R.; “Ferroalloys and Alloying Additives HANDBOOK, Shieldalloy Corp, 1981, http://amg-v.com/contents.html

[19] Azo Materials. ‘Analysis of Microalloying Elements in Steel” 2020

[20] Pietrzyk, M.; Madej, L.; Rauch, L.; Szeliga, D.; “Computational Materials Engineering: Achieving High Accuracy and Efficiency in Metals Processing Simulations” ISBN 978-0-12-416707-0

[21] Qingshen Ma et al; “Effect of Microalloying Elements on Microstructure and Properties of Quenched and Tempered Constructional Steel” 2017 IOP Conference Series: Materials Science and Engineering 242 012036

[22] Diehl Tool Steel; https://www.diehlsteel.com/technical-information/effects-of-common-alloying-elements-in-steel

[23] Väyrynen, P.; Holappa, L.; and Louhenkilpi, S.; “Simulation of Melting of Alloying Materials in Steel Ladle”

[24] Peaslee, K. D.; Webber, D. S.; Randall, B.; “Alloy Recovery and Control in Steel Making” Scholar’s Mine 2005 Materials Science and Engineering

[25] Duan, H.; Zhang, L.; Thomas, B. G.; “Effect of Melt Superheat and Alloy Size on the Mixing Phenomena in Argon-Stirred Steel Ladles” Steel Research International / Volume 90, Issue 4 / 1800288

[26] Argyropoulos, S.; Guthrie, R.; "Dissolution Kinetics of Ferroalloys in Steelmaking." 65th Steelmaking Conference Proceedings, Iron and Steel Society, Vol. 65 (1982). 156-167

[27] Sripriya, R.; Murty, Ch.V.G.K.; "Recovery of Metal from Slag/Mixed Metal Generated in Ferroalloy Plants - A Case Study" International Journal of Mineral Processing Volume 75, Issues 1–2, 6 January 2005, Pages 123-134

[28] Duan, H.; Zhang, L.; Thomas, B. G.; Conejo A. N.; "Fluid Flow, Dissolution, Mixing Phenomena in Argon-Stirred Steel Ladles" The Minerals, Metals & Materials Society and ASM International 2018; https://doi.org/10.1007/s11663-018-1350-4

[29] Chen, G.; He, S.; Li, Y.; "Investigation of the Air-Argon-Steel-Slag Flow in an industrial RH Reactor with VOF-DPM Coupled Model"

[30] ANSYS Fluent guide

[31] Aoki, J.; Thomas, B.G.; Peter, J.; Peaslee, K.D.; "Experimental and Theoretical Investigation of Mixing in a Bottom Gas-Stirred Ladle" AISTech Proceedings, 2004.

[32] Haider A.; Levenspiel, O.; "Drag Coefficient and Terminal Velocity of Spherical and Nonspherical Particles", Powder Technology, Vol. 58, 1989, pp.63-70

[33] Whitaker, S.; "Forced Convection Heat Transfer Correlations for Flow in Pipes, Past Flat Plates, Single Cylinders, Single Spheres, and for Flow in Packed Beds and Tube Bundles", A. I. Ch. E. Journal, Vol. 18, Issue 2, 1972, pp. 361-371

[34] Engh, T. A.; "Principles of Metal Refining", Oxford Science Publications

[35] Sismanis, P.G.; "The Dissolution of Niobium and Zirconium in Liquid Steel"; National Library of Canada

[36] Cruz, E. B.; Fridman, D. P.; Carboni. M.C.; Guimaraes, R.C.; Nogueira, M. A. S.; "Dissolution of FeNb in Liquid Steel" Fundamentals and Applications of Mo and Nb Alloying in High Performance Steels - Volume 2; CBMM, IOMA and TMS, 2015.

[37] Mazumdar, D. and Guthrie, R. "Mixing Times and Correlations for Gas Stirred Ladle Systems." Iron and Steel Society Transactions, Vol. 26 No. 9 (1999): 89-96.